Article

Atomic Data Assessment with PyNeb: Radiative and Electron Impact Excitation Rates for [Fe II] and [Fe III]

Claudio Mendoza [1,*], José E. Méndez-Delgado [2], Manuel Bautista [3], Jorge García-Rojas [4,5] and Christophe Morisset [6]

[1] Physics Center, Venezuelan Institute for Scientific Research (IVIC), Caracas 1020, Venezuela
[2] Astronomisches Rechen-Institut, Zentrum für Astronomie der Universität Heidelberg, D-69120 Heidelberg, Germany; jemd@uni-heidelberg.de
[3] Department of Physics, Western Michigan University, Kalamazoo, MI 49008, USA; manuel.bautista@wmich.edu
[4] Instituto de Astrofísica de Canarias (IAC), E-38205 La Laguna, Spain; astroyorch@gmail.com
[5] Departamento de Astrofísica, Universidad de La Laguna, E-38206 La Laguna, Spain
[6] Instituto de Astronomía, Universidad Nacional Autónoma de México, Ensenada 22860, Mexico; chris.morisset@gmail.com
* Correspondence: claudiom07@gmail.com; Tel.: +1-269-370-8465

Abstract: We use the `PyNeb` 1.1.16 Python package to evaluate the atomic datasets available for the spectral modeling of [Fe II] and [Fe III], which list level energies, *A*-values, and effective collision strengths. Most datasets are reconstructed from the sources, and new ones are incorporated to be compared with observed and measured benchmarks. For [Fe III], we arrive at conclusive results that allow us to select the default datasets, while for [Fe II], the conspicuous temperature dependency on the collisional data becomes a deterrent. This dependency is mainly due to the singularly low critical density of the $3d^7\,a\,^4F_{9/2}$ metastable level that strongly depends on both the radiative and collisional data, although the level populating by fluorescence pumping from the stellar continuum cannot be ruled out. A new version of `PyNeb` (1.1.17) is released containing the evaluated datasets.

Keywords: nebular modeling; astrophysical software; plasma diagnostics; atomic databases; atomic data assessment

Citation: Mendoza, C.; Méndez-Delgado, J. E.; Bautista, M.; García-Rojas, J.; Morisset, C. Atomic Data Assessment with PyNeb: Radiative and Electron Impact Excitation Rates for [Fe II] and [Fe III]. *Preprints* **2023**, *1*, 0. https://doi.org/

Academic Editor: Alexander Kramida

1. Introduction

`PyNeb`[1] [1,2] is a widely used Python tool for the analysis of emission lines in nebular plasmas to determine the temperature, density, and chemical abundances [3]. It essentially solves the equations of statistical equilibrium by addressing an extensive atomic database of radiative and collisional rates; therefore, `PyNeb`'s diagnostic potential relies directly on the accuracy of this database. In this respect, its data curation strategy is based on the selection of recommended default datasets and keeping access to a historical archive of radiative and collisional files rather than discarding them. This singular scheme allows modelers to estimate the uncertainties of the plasma diagnostics and chemical abundances due to the scatter of the atomic parameters. It also provides a versatile environment for atomic data assessment, which has been previously used productively to benchmark the accuracy of the radiative rates in N- and P-like ions and effective collision strengths in C-like ions [4] and to determine the atomic-data impact on density diagnostics [5].

As a follow-up to [4], we apply `PyNeb`'s capabilities to assess the radiative and collisional rates associated with the transition arrays of [Fe II] and [Fe III]. These ions give rise to forbidden lines in the optical and infrared spectra of H II regions, planetary nebulae, and quasars that are used to determine plasma conditions and iron abundance, the latter particularly in the context of depletion factors in the life cycle of dust grains [6–8]. These iron transition arrays are also useful for studying the shocked plasma caused by outflows from newborn stars that form bright Herbig–Haro (HH) objects perturbing stellar accretion [9–11]. The high-resolution

spectra of such HH objects—e.g., HH 202S [9] and HH 204 [11] in the Orion Nebula—taken with the Ultraviolet Visual Echelle Spectrograph (range 3100–10,400 Å) [12] present an observational opportunity to benchmark the Fe II and Fe III atomic data. The optical emission spectra of these two HH objects are dominated by photoionization from θ^1 Ori C, the main ionization source of the Orion Nebula, and can therefore be treated as small-scale H II regions [10].

Due to the astrophysical importance of Fe II, the computation of radiative and collisional rates for the spectral modeling of this system has received considerable attention since the early semi-empirical computations of A-values (radiative transition probabilities) for the forbidden [13] and dipole-allowed [14] transitions and electron-impact collision strengths with the distorted wave method [15,16]. Our intention here is not to evaluate this vast body of data but to concentrate on complete and accurate datasets to model the spectra of [Fe II] and [Fe III] observed in nebular plasmas.

A landmark systematic effort to compute radiative and collisional data for the fine-structure spectral modeling of Fe ions was undertaken by the Iron Project[2] using the R-matrix method [17] and relativistic multi-configuration structure codes such as SUPERSTRUCTURE [18], CIV3 [19], and HFR [20]. For Fe II and Fe III, A-values were computed for both allowed and forbidden lines [21–23] and electron-impact effective collision strengths (ECS) for infrared, optical, and ultraviolet transitions [24–26]. Although these R-matrix calculations were originally performed in LS coupling followed by algebraic transformations to intermediate coupling, more recent scattering calculations for these ionic species [27–31] have relied on R-matrix implementations based on the Breit–Pauli Hamiltonian (BPRM [32], BSR [33]) and Dirac–Fock Hamiltonian (DARC [34]). In some cases, e.g., the collisional excitation of levels within the Fe^+ ground configuration, low-temperature ECS have been computed with several R-matrix implementations—intermediate coupling frame transformation (ICFT, [35]), BPRM, and DARC—to obtain uncertainty estimates [36].

Extensive multi-configuration Breit–Pauli (MCBP) calculations of gf-values (weighted oscillator strengths) and A-values for allowed and forbidden transitions in Fe II and Fe III [37–43] with the code CIV3 have shown that fine-tuning corrections to the Hamiltonian matrix by fitting to the experimental level energies lead to more accurate configuration expansions. However, significant A-value differences (greater than 20–30%) are found for some transitions computed with comparable multi-configuration methods that also implement fine-tuning corrections (e.g., [23,44,45]), which are caused by strong configuration mixing, double-excitation representations, and subtle core–valence correlation involving the closed $3p^6$ and open $3d^n$ subshells.

Since the Fe II radiative data display a large scatter, experimentalists and astronomical observers have been enticed to measure accurate radiative parameters such as lifetimes and branching fractions to determine A- and gf-values; however, most of them address allowed transitions involving odd-parity states. Lifetimes have been measured for 21 Fe II levels with a time-resolved nonlinear laser-induced fluorescence technique to an accuracy of 2–3%, and by means of branching fractions, absolute A-values were reported to be within 6% and 26% for the strong and weak transitions, respectively [46]. Accurate gf-values for 142 Fe II lines were determined from laboratory and solar spectroscopic multiplets and theoretical fine-structure ratios, assuring that oscillator-strength error no longer hinders stellar abundance studies [47]. Branching fractions have been measured for 121 ultraviolet Fe II lines (2250–3280 Å), and through published lifetimes, gf-values have been derived and applied to iron abundance determinations in the Sun and the metal-poor star HD 84937 [48]. Good agreement is obtained with the Fe standard solar abundance. On the other hand, the only lifetime measurements of [Fe II] even-parity metastable states to derive transition probabilities have been carried out by the Ferrum Project using a laser probing technique on a stored ion beam, the branching fractions being derived from astrophysical spectra [49–51]. Consistent differences

between the observed intensity ratios and theoretical branching fractions have suggested that the [Fe II] lines might be used to determine reddening.

In the present data assessment, we revise the Fe II and Fe III atomic datasets—namely, energy levels, A-values, and ECS—available in `PyNeb` 1.1.16. In most cases, we reconstruct the atomic models from the sources by mapping the rates to the NIST level structure. We renormalize the number of levels to a predefined value to enable one-to-one comparisons among the theoretical datasets and benchmarks with the HH 202S and HH 204 spectra and the aforementioned experimental data. We also extend the `PyNeb` database with additional new datasets, the main objective being the default selection for a new version: `PyNeb` 1.1.17.

We give a brief description of `PyNeb`'s file structure and methods in Section 2, and carry out the data assessments and discussions of Fe III and Fe II in Sections 3 and 4 followed by the conclusions in Section 5.

2. PyNeb

A brief description of the `PyNeb` package is given in [4], in particular of its object-oriented architecture. The ion object is thereby represented by the `Atom` class, offering a set of methods through the `atomicData` manager. Regarding energy levels, A-values, and ECS, `PyNeb` has three file types:

- *xxx*`_levels.dat`: lists NIST energy levels for ionic species *xxx*;
- *xxx*`_atom_`*ref*`.dat`: lists A-values for transitions between energy levels of ion *xxx* contained in the *ref* dataset;
- *xxx*`_coll_`*ref*`.dat`: lists ECS for transitions between energy levels of ion *xxx* contained in the *ref* dataset.

A printout of the NIST energy levels for a specific ion, Fe III say, may be obtained with the function `getLevelsNIST()`:

```
# Call thePyNeb Python module
import pyneb as pn
# List NIST energy levels for Fe III
levels = pn.getLevelsNIST('Fe3')
print(levels)
```

and a list of all the Fe III `atom` and `coll` files is currently available with:

```
pn.atomicData.getAllAvailableFiles('Fe3')
```

```
['* fe_iii_atom_Q96_J00.dat',
 '* fe_iii_coll_Z96.dat',
 'fe_iii_atom_BBQ10.dat',
 'fe_iii_atom_NP96.dat',
 'fe_iii_coll_BB14.dat',
 'fe_iii_coll_BBQ10.dat']
```

where the recommended default files are prefixed with an asterisk. Alternative files may be easily accessed by the user to replace the default files with the function

```
pn.atomicData.setDataFile('fe_iii_atom_BBQ10.dat')
pn.atomicData.setDataFile('fe_iii_coll_BBQ10.dat')
```

We can now instantiate the Fe III ion with the new atomic datasets

```
pn.atomicData.getDataFile('Fe3')
Fe3=pn.Atom('Fe',3,NLevels=34)
```

and apply a series of methods to determine some of its plasma properties:

```
# Emissivity for transition 2-1 at T = 1.0e4 K and n_e = 1.0e4 cm-3
Fe3.getEmissivity(tem=1.0e4,den=1.0e4,lev_i=2,lev_j=1)
# Emissivity for transition with wavelength 4658.17 A at T = 1.0e4 K
# and n_e = 1.0e4 cm-3
Fe3.getEmissivity(tem=1.0e4,den=1.0e4,wave=4658.17)
# Level critical densities at T = 1.0e4 K
Fe3.getCritDensity(1.0e4)
# Level populations at T = 1.0e4 K and n_e = 1.0e4 cm-3
Fe3.getPopulations(tem=1.0e4, den=1.0e4)
```

In the ion instantiating command above, the option `NLevels` specifies the number of levels of the atomic model, which can be the total (default) or a reduced set.

A complete list of methods is included in the `PyNeb` manual. The `Atom` class also addresses the ion atomic properties, e.g., the ECS at a selected temperature

```
# Collision strength for transition 2-1 at T = 1.0e4 K
Fe3.getOmega(1.0e4,2,1)
```

This function is useful as it returns the interpolated value at the prescribed input temperature allowing comparisons between different ECS datasets with tabulations on diverse temperature ranges. The original temperature and ECS arrays may be listed with the commands

```
# Temperature and collision strength original arrays
Fe3.getTemArray()
Fe3.getOmegaArray()
```

3. Fe III

3.1. *Fe* III *Atomic Datasets in PyNeb*

Fe III atomic models in `PyNeb` 1.1.16 comprise 34 fine-structure levels (energy $E < 60,000\,\mathrm{cm}^{-1}$) from the $3d^6$ and $3d^5 4s$ electron configurations, whose attributes were obtained from the NIST server (April 2017). Levels $3d^6$ b $^1D_2$ and b $^1S_0$ at $E > 77,000\,\mathrm{cm}^{-1}$ are therefore not taken into account, and from the $3d^5 4s$ configuration, only the lowly lying $^7S_3$ and $^5S_2$ are included. Transitions among the levels of these two even-parity configurations are electric dipole (E1) forbidden and thus occur via electric quadrupole (E2) and magnetic dipole (M1) operators. Shortcomings in the spectral fits resulting from the number of levels in the atomic models, 34 levels in this case, will be examined by comparing with extended models of 144 levels (see Section 3.2).

Two fundamental interactions in the computation of accurate radiative (A-values) and collisional (ECS) rates for atomic ions are electron correlation (configuration interaction, CI) and relativistic coupling. We give below brief descriptions of the numerical methods and approximations that were used to compute the datasets available in `PyNeb` 1.1.16.

atom_NP96 —Contains A-values for E2 and M1 transitions computed in an extensive CI framework with the multi-configuration Breit–Pauli (MCBP) code SUPERSTRUCTURE [22].

coll_Z96 —ECS were calculated in an 83-term non-relativistic *R*-matrix calculation including the $3d^6$, $3d^5 4s$, and $3d^5 4p$ configurations. ECS for 219 fine-structure levels were then obtained through algebraic recoupling [25].

atom_Q96_J00 —The Pauli Hartree–Fock HFR code was used to compute *A*-values for the radiative transitions within the $3d^6$ configuration [44]. Wave functions were generated with CI expansions adjusting the electrostatic and spin–orbit integrals to fit the spectroscopic level energies. *A*-values for the $3d^5 4s\ ^7S_3$ and $^5S_2$ levels were obtained independently with HFR using empirically adjusted Slater parameters [52].

atom_BBQ10, coll_BBQ10 —A 36-configuration CI expansion including pseudo-orbitals ($\overline{4f}$, $\overline{5s}$, $\overline{5p}$, and $\overline{5d}$) was used to compute *A*-values with the MCBP AUTOSTRUCTURE atomic structure code [27,53]. Term-energy corrections were introduced to fine-tune the wave functions. ECS were computed with the Dirac–Coulomb *R*-matrix package (DARC) based on a 3-configuration target constructed with the GRASP92 multi-configuration Dirac–Hartree–Fock structure code [54] under the extended average level approximation.

coll_BB14 —ECS were computed with the ICFT *R*-matrix method using a 136-term (322 fine-structure levels) target representation [28]. This MCBP 3-configuration target was generated with AUTOSTRUCTURE using a Thomas–Fermi–Dirac–Amaldi model potential.

3.2. Fe III *Revised and New Atomic Datasets*

The present work intends to revise the datasets currently available in `PyNeb`, incorporate new ones, and implement procedures for data evaluation. For such purposes, we have collected the data from the original sources, verified consistency, and implemented new `atom` and `coll` files. To begin with, we have introduced a new level file, `fe_iii_levels.dat`, with updated spectroscopic measurements (improved accuracy and new levels such as $3d^6\ b\ ^1D_2$) from the NIST database (July 2022) [55]. We list below the revised and new atomic datasets with brief descriptions; the suffix "_*n*" is now appended to the dataset label, where *n* is the number of levels in the atomic model. For data comparisons, we have normalized all Fe III datasets to 34 levels, but to estimate model convergence, we have extended some models to 144 levels.

An important issue is how to deal with missing energy levels in both the theoretical and spectroscopic reports since the `PyNeb` energy-level files are based on the NIST database, which is incomplete at the higher energies. In spectrum modeling, levels with zero decay rates may lead to numerical problems; we have, therefore, limited the number of levels in the atomic models to those that have been both computed and measured. From the user's point of view, modeling turnaround time is also an important issue; therefore, the number of levels in the atomic models must take this point into consideration.

atom_Q96_34 —The main differences with the atom_Q96_J00 dataset described in Section 3.1 are the *A*-values for transitions involving the $3d^5 4s\ ^7S_3$ and $^5S_2$ levels. The radiative rates in atom_Q96_J00 for transitions decaying from the $^7S_3$ upper level are set to $A = 0.0$, while those from $^5S_2$ were calculated with HFR with empirically adjusted Slater parameters [52]. In this dataset, radiative rates for transitions involving these levels have been updated with *A*-values from atom_BB14_34. This choice is to a certain extent arbitrary as inferred from the wide *A*-value scatter shown for the transitions $^5S_2 - {}^5D_J$ in Table 1. We include in this comparison *A*-values computed with extensive CI using both HFR and AUTOSTRUCTURE (atom_FBQh16 and atom_FBQa16) [45]; however, these datasets lack the completeness required to model collisionally excited nebular lines and, consequently, will not be further considered in the present data assessment.

Table 1. A-value comparison for the $3d^5 4s\ ^5S_2 - 3d^6\ ^5D_J$ transitions in [Fe III]. A-values in J00 were calculated with the semi-relativistic HFR code using empirical Slater parameters [52] and included in the atom_Q96_J00 dataset (see Section 3.1). The methods used to compute the radiative data in atom_BBQ10_34 and atom_BB14_34 are described below. A-values in atom_FBQh16 and atom_FBQa16 were, respectively, computed with HFR and AUTOSTRUCTURE with extensive CI [45].

J	λ_{air} (Å)	A-Value (s^{-1})				
		J00	**BBQ10_34**	**BB14_34**	**FBQh16**	**FBQa16**
4	2438.28	22.2	25.7	38.4	32.0	31.6
3	2464.48	16.0	18.7	28.0	23.3	23.1
2	2483.01	11.0	12.8	19.1	15.9	15.8
1	2495.01	6.4	7.43	11.1	9.29	9.22
0	2500.93	2.0	2.44	3.66		

coll_Z96_34 —ECS listed in the supplementary data associated with the original publication [25] were downloaded directly from the CDS to build a new file (see Section 3.1 for details of the calculation).

coll_Z96_144 —The coll_Z96_34 dataset was extended to include 144 levels from the $3d^6$, $3d^5 4s$, and $3d^5 4p$ configurations with $E < 121,500\,cm^{-1}$. For higher energies, inconsistencies in the reported list of measured and computed levels begin to appear. Although this model extension is not expected to contribute to the collisionally excited nebular lines, it may be relevant if the populations of the $3d^5 4p$ levels generate E1 arrays.

atom_DH09_34 —A-values for the E2 and M1 transitions between levels of the $3d^6$ configuration have been computed with the MCBP code CIV3 [19,56] in a CI scheme spanning single and double excitations [38]. To improve accuracy, the diagonal elements of the Hamiltonian matrix were fine-tuned to fit the experimental energies. Similarly to atom_Q96_34, A-values for transitions involving the $3d^5 4s\ ^7S_3$ and $^5S_2$ levels are taken from atom_BB14_34.

atom_BBQ10_34, coll_BBQ10_34 —A-values and ECS were downloaded from the XSTAR database [57], and the `PyNeb` `atom` and `coll` files were rebuilt.

atom_BB14_34, coll_BB14_34 —Computed A-values and ECS were obtained from the `crlike_nrb13#fe2.dat` `adf04` file downloaded from the OPEN-ADAS[3] database. Details of the ECS computation [28] are described in Section 3.1. No information is given in the `adf04` file on the provenance of the radiative data; thus, we assume they are coproducts of the target calculation.

atom_BB14_144, coll_BB14_144 —The BB14_34 model has been extended to include 144 levels from the $3d^6$, $3d^5 4s$, and $3d^5 4p$ configurations with $E < 121,500\,cm^{-1}$.

3.3. Fe III Observational Benchmarks

3.3.1. A-Value Ratio Benchmark

It is well known that the intensity ratio of two spectral lines arising from a common upper level can be expressed as

$$\frac{I(j,i)}{I(j,i')} = \frac{A(j,i)}{A(j,i')} \times \frac{\lambda(j,i')}{\lambda(j,i)} \tag{1}$$

enabling an observational benchmark of the theoretical A-value ratio $A(j,i)/A(j,i')$. This measure provides indications of the accuracy of both the observed intensities and computed radiative rates, signposting unreliable lines to be excluded from the spectrum fits.

In Tables 2 and 3, we compare the observed line-intensity ratios from HH 202S and HH 204 [9,11] with the A-value ratios from the BBQ10_34, BB14_34, DH09_34, and Q96_34

atom files. The relative uncertainties in the observed intensity ratios from HH 202S are, in general, larger than those from HH 204. Although both spectra are of comparable quality, HH 204 was observed under photometric conditions whereby the absolute calibration error is slightly smaller; moreover, the HH 204 integrated emission comprised twice the area of HH 202S with longer exposure times.

For both sources, the observed intensity ratios for transitions arising from levels $3d^6\ a\ ^3F_J$ or lower and ending up at a level within the ground configuration $3d^6\ a\ ^5D$ with wavelengths $\lambda > 4600$ Å are generally more accurate (better than 15%). For transitions arising from higher levels, uncertainties as large as 70% have been listed. On the other hand, most theoretical ratios agree to within 10% except for significantly discrepant cases in atom_BBQ10_34: $I(\lambda 3286)/I(\lambda 8729)$; $I(\lambda 3366)/I(\lambda 9960)$; and $I(\lambda 3357)/I(\lambda 8838)$. As a whole, the theoretical ratios lie within the observed ratio error bars except for some questionable lines in HH 202S ($\lambda 8729$, affected by telluric absorptions) and in HH 204 ($\lambda\lambda 4080, 4097$ blended with O II lines and $\lambda\lambda 7078, 7088, 9204$ being misidentifications).

Table 2. Comparison of observed [Fe III] line intensity ratios in HH 202S (Obs) for transitions sharing a common upper level with those estimated from the A-values in the BBQ10_34, BB14_34, DH09_34, and Q96_34 atom files. The error of the least significant figure of the observed intensity ratio is indicated in brackets.

Line 1			Line 2		Obs	BBQ10_34	BB14_34	DH09_34	Q96_34
Upper	**Lower**	**λ_{air}(Å)**	**Lower**	**λ_{air}(Å)**	**Line Intensity Ratio**				
$3d^6\ ^3D_3$	$3d^6\ ^5D_4$	3239.79	$3d^6\ ^5D_3$	3286.24	4(1)	3.58	3.59	3.28	3.60
$3d^6\ ^3D_3$	$3d^6\ ^5D_3$	3286.24	$3d^6\ a\ ^3P_2$	8728.84	2.0(5)	4.88	3.12	3.80	3.29
$3d^6\ ^3D_1$	$3d^6\ ^5D_1$	3355.50	$3d^6\ ^5D_0$	3366.22	1.6(8)	1.13	1.12	1.16	1.14
$3d^6\ ^3D_1$	$3d^6\ ^5D_0$	3366.22	$3d^6\ a\ ^3P_1$	9959.85	5(4)	9.07	5.42	6.37	5.54
$3d^6\ ^3D_2$	$3d^6\ ^5D_2$	3334.95	$3d^6\ ^5D_1$	3356.59	1.2(2)	1.14	1.15	1.20	1.18
$3d^6\ ^3D_2$	$3d^6\ ^5D_1$	3356.59	$3d^6\ a\ ^3P_2$	8838.14	4.1(8)	6.01	4.28	4.39	4.19
$3d^5 4s\ ^7S_3$	$3d^6\ ^5D_4$	3322.47	$3d^6\ ^5D_3$	3371.35	1.4(3)	1.38	1.37		
$3d^5 4s\ ^7S_3$	$3d^6\ ^5D_3$	3371.35	$3d^6\ ^5D_2$	3406.11	2.2(5)	2.33	2.31		
$3d^6\ ^3G_3$	$3d^6\ ^5D_3$	4046.49	$3d^6\ ^5D_2$	4096.68	2.3(8)	2.27	2.45	2.56	2.53
$3d^6\ ^3G_4$	$3d^6\ ^5D_4$	4008.34	$3d^6\ ^5D_3$	4079.69	3.8(7)	3.15	3.63	3.62	3.92
$3d^6\ a\ ^3F_2$	$3d^6\ ^5D_3$	4667.11	$3d^6\ ^5D_2$	4734.00	0.29(4)	0.28	0.28	0.29	0.28
$3d^6\ a\ ^3F_2$	$3d^6\ ^5D_2$	4734.00	$3d^6\ ^5D_1$	4777.70	2.0(3)	2.06	2.07	2.09	2.08
$3d^6\ a\ ^3F_3$	$3d^6\ ^5D_4$	4607.12	$3d^6\ ^5D_3$	4701.64	0.19(3)	0.18	0.18	0.19	0.17
$3d^6\ a\ ^3F_3$	$3d^6\ ^5D_3$	4701.64	$3d^6\ ^5D_2$	4769.53	2.8(3)	2.89	2.90	2.93	2.94
$3d^6\ a\ ^3F_4$	$3d^6\ ^5D_4$	4658.17	$3d^6\ ^5D_3$	4754.81	5.3(6)	5.28	5.40	5.32	5.49
$3d^6\ a\ ^3P_1$	$3d^6\ ^5D_2$	5011.41	$3d^6\ ^5D_0$	5084.85	5.9(9)	5.72	6.12	5.97	5.95
$3d^6\ ^3H_4$	$3d^6\ ^5D_4$	4881.07	$3d^6\ ^5D_3$	4987.29	5.4(7)	4.99	5.33	5.50	5.76
$3d^6\ a\ ^3P_2$	$3d^6\ ^5D_3$	5270.57	$3d^6\ ^5D_1$	5412.06	11(2)	10.2	11.4	11.4	11.0

Table 3. Comparison of observed [Fe III] line intensity ratios in HH 204 (Obs) for transitions sharing a common upper level with those estimated from *A*-values in the BBQ10_34, BB14_34, DH09_34, and Q96_34 `atom` files. The error of the least significant figure of the observed intensity ratio is indicated in brackets.

Line 1			Line 2		Obs	BBQ10_34	BB14_34	DH09_34	Q96_34
Upper	**Lower**	**λ_{air}(Å)**	**Lower**	**λ_{air}(Å)**	**Line Intensity Ratio**				
$3d^6\ ^3D_3$	$3d^6\ ^5D_4$	3239.79	$3d^6\ ^5D_3$	3286.24	3.6(9)	3.58	3.59	3.28	3.60
$3d^6\ ^3D_3$	$3d^6\ ^5D_3$	3286.24	$3d^6\ ^5D_2$	3319.27	1.0(4)	1.35	1.36	1.47	1.41
$3d^6\ ^3D_3$	$3d^6\ ^5D_2$	3319.27	$3d^6\ a\ ^3P_2$	8728.84	3.1(8)	3.62	2.30	2.59	2.35
$3d^6\ ^3D_1$	$3d^6\ ^5D_1$	3355.50	$3d^6\ ^5D_0$	3366.22	1.5(3)	1.13	1.12	1.16	1.14
$3d^6\ ^3D_2$	$3d^6\ ^5D_2$	3334.95	$3d^6\ ^5D_1$	3356.59	1.2(3)	1.14	1.15	1.20	1.18
$3d^6\ ^3D_2$	$3d^6\ ^5D_1$	3356.59	$3d^6\ a\ ^3P_2$	8838.14	5.3(7)	6.01	4.28	4.39	4.19
$3d^6\ ^1I_6$	$3d^6\ ^3H_6$	9701.87	$3d^6\ ^3H_5$	9942.38	1.4(2)	1.58	1.54	1.56	1.55
$3d^5 4s\ ^7S_3$	$3d^6\ ^5D_4$	3322.47	$3d^6\ ^5D_3$	3371.35	1.5(2)	1.38	1.37		
$3d^5 4s\ ^7S_3$	$3d^6\ ^5D_3$	3371.35	$3d^6\ ^5D_2$	3406.11	1.7(2)	2.33	2.31		
$3d^6\ ^3G_3$	$3d^6\ ^5D_3$	4046.49	$3d^6\ ^5D_2$	4096.68	3.4(9)	2.27	2.45	2.56	2.53
$3d^6\ ^3G_4$	$3d^6\ ^5D_4$	4008.34	$3d^6\ ^5D_3$	4079.69	4.4(4)	3.15	3.63	3.62	3.92
$3d^6\ a\ ^3F_2$	$3d^6\ ^5D_3$	4667.11	$3d^6\ ^5D_2$	4734.00	0.29(1)	0.28	0.28	0.29	0.28
$3d^6\ a\ ^3F_2$	$3d^6\ ^5D_2$	4734.00	$3d^6\ ^5D_1$	4777.70	2.1(1)	2.06	2.07	2.09	2.08
$3d^6\ a\ ^3F_3$	$3d^6\ ^5D_4$	4607.12	$3d^6\ ^5D_3$	4701.64	0.18(1)	0.18	0.18	0.19	0.17
$3d^6\ a\ ^3F_3$	$3d^6\ ^5D_3$	4701.64	$3d^6\ ^5D_2$	4769.53	2.9(1)	2.89	2.90	2.93	2.94
$3d^6\ a\ ^3F_4$	$3d^6\ ^5D_4$	4658.17	$3d^6\ ^5D_3$	4754.81	5.3(2)	5.28	5.40	5.32	5.49
$3d^6\ a\ ^3P_1$	$3d^6\ ^5D_2$	5011.41	$3d^6\ ^5D_0$	5084.85	5.9(4)	5.72	6.12	5.97	5.95
$3d^6\ ^3H_4$	$3d^6\ ^5D_4$	4881.07	$3d^6\ ^5D_3$	4987.29	6.1(2)	4.99	5.33	5.50	5.76
$3d^6\ a\ ^3P_2$	$3d^6\ ^5D_3$	5270.57	$3d^6\ ^5D_1$	5412.06	10.8(5)	10.2	11.4	11.4	11.0

3.3.2. [Fe III] Spectrum Fits

Following [4], we take advantage of `PyNeb`'s methods for emission-line modeling to implement a further observational benchmark to assess the accuracy of the atomic datasets described in Sections 3.1 and 3.2. For this purpose, we again use the high-resolution spectra of the bright HH 202S and HH 204 sources.

The electron temperature and density of the HH object are obtained by a least-squares fit of all the reliable spectral lines as proposed by [58]. The theoretical emissivity and observed intensity of each line are respectively normalized with respect to the emissivity and intensity sums of the transition array. The fit measure is given in terms of

$$\chi^2 = \sum_{i=1}^{N} \frac{(I_i - \epsilon_i)^2}{N\sigma_{I_i}^2}\,, \tag{2}$$

where N is the number of spectral lines, I_i and ϵ_i are the normalized intensity and emissivity, respectively, and $\sigma_{I_i}^2$ is the variance of the normalized intensity [59]. No explicit error is considered in the theoretical emissivities. The least-squares minimization is carried out with the Python function `scipy.optimize.minimize` finding no degeneracies in the χ^2 convergence.

`PyNeb` provides two methods to compute the emissivity of a spectral line (e.g., λ5270.57 between levels $i = 6$ and $j = 2$ of Fe III) at (T_e, n_e) by addressing, say, the datasets atom_Q96_J00 and coll_Z96. The Python commands to run these two methods (`e1` and `e2`) are as follows:

```
# Call the PyNeb Python module
import pyneb as pn
# Select the radiative and collisional datasets
pn.atomicData.setDataFile('fe_iii_atom_Q96_J00.dat')
pn.atomicData.setDataFile('fe_iii_coll_Z96.dat')
# Instantiate Fe III
Fe3=pn.Atom('Fe',3)
# Check the datafiles
print(Fe3)
# Determine and print the two emissivities
e1=Fe3.getEmissivity(tem=1.e4,den=1.0e4,wave=5270.57)
e2=Fe3.getEmissivity(tem=1.e4,den=1.0e4,lev_i=6,lev_j=2)
print(e1,e2)
```

In the present work, consistency between `e1` and `e2` for the whole spectrum was tested to avoid incorrect line identifications, but we found that `e2` avoided the problem of transitions with the same wavelength in atomic models with a large number of levels.

In the spectrum fits of HH 202S and HH 204, a handful of lines are excluded due to the following problems:

- Misidentifications: $\lambda\lambda$7078, 7088, 9204
- Line blending or telluric contamination [9]: $\lambda\lambda$4080, 4097, 4925, 4931, 4987, 8729, 8838
- Small A-values ($\lesssim 10^{-3}$ s^{-1}): $\lambda\lambda$4008, 4047.

We first examine in Table 4 the spectral fits with the atomic datasets available in `PyNeb` 1.1.16 (see Section 3.1). For each `coll` dataset BBQ10, BB14, and Z96, we run the fits in turn with three `atom` datasets: BBQ10, NP96, and Q96_J00. For HH 202S, we obtain an average temperature and density of $T_e = (7 \pm 1) \times 10^3$ K and $n_e = (6 \pm 5) \times 10^4$ cm^{-3}, which indicate large uncertainties due to the atomic data. In particular, coll_BB14 gives, on average, a questionable low temperature (5.4×10^3 K) and high density (1.3×10^5 cm^{-3}). The quality of the fits is generally poor,

the best being atom_BBQ10–coll_Z96 with $\chi^2 = 1.74$. The fits for HH 204 are as unimpressive: $T_e = (8 \pm 2) \times 10^3$ K) and $n_e = (5 \pm 4) \times 10^4$ cm^{-3}, the best ($\chi^2 = 16.9$) being with the file pair atom_BBQ10–coll_Z96.

Table 4. Temperature and density fits of the [Fe III] observed spectra of HH 202S and HH 204 with the radiative (`atom`) and collisional (`coll`) datasets available in `PyNeb` 1.1.16.

Datasets		HH 202S			HH 204		
Atom	**Coll**	T_e **(10^3 K)**	n_e **(10^4 cm^{-3})**	χ^2	T_e **(10^3 K)**	n_e **(10^4 cm^{-3})**	χ^2
BBQ10	BBQ10	7.99	1.92	12.0	9.77	1.53	66.9
NP96	BBQ10	8.37	3.79	13.9	10.5	2.24	57.2
Q96_J00	BBQ10	7.80	1.96	14.4	9.60	1.36	58.1
BBQ10	BB14	5.26	13.1	14.9	5.95	11.3	88.7
NP96	BB14	5.54	16.8	15.3	6.15	10.5	60.2
Q96_J00	BB14	5.26	8.54	15.8	5.95	5.51	60.4
BBQ10	Z96	7.34	2.52	1.74	8.53	1.70	16.9
NP96	Z96	7.44	7.09	15.2	9.54	4.20	69.9
Q96_J00	Z96	7.35	2.55	12.0	8.79	1.68	37.7

In a similar fashion, we proceed to benchmark the revised and new datasets described in Section 3.2 by running a grid of fits with different `atom-coll` file pairs: four radiative and three collisional datasets (see Table 5). The improvement is considerable; the average temperature and density for HH 202S is now $T_e = (7.9 \pm 0.3) \times 10^3$ K and $n_e = (2.1 \pm 0.3) \times 10^4$ cm^{-3} and for HH 204 $T_e = (8.9 \pm 0.6) \times 10^3$ K and $n_e = (1.5 \pm 0.3) \times 10^4$ cm^{-3}. Outstanding fits for HH 202S are obtained with the atom_DH09_34–coll_Z96_34 and atom_Q96_34–coll_Z96_34 dataset pairs, and the revised coll_BB14_34 ECS dataset now gives more reasonable temperatures ($\sim 8 \times 10^3$ K) and densities ($\sim 2 \times 10^4$ cm^{-3}). We find questionable ECS differences between coll_BB14 and coll_BB14_34 for transitions involving levels a ^{3}P$_J$, a ^{3}F$_J$, and a ^{1}G$_4$; furthermore, for levels with $E > 43{,}000$ cm^{-1}, the ECS in coll_BB14 are $\Upsilon(j,i) = 0.0$. We also found ECS differences for transitions to level 3d^{5}4s ^{7}S$_3$ in coll_BBQ10 and coll_BBQ10_34 due to improvements performed by [27] after publication. On the other hand, the extended datasets atom_BB14_144, coll_BB14_144, and coll_Z96_144, as expected, make no difference in these plasma conditions.

The temperature and density scatters are now within 6% and 20%, respectively, and our average values compare satisfactorily with those adopted in the observational papers [9,11]: $T_e = (8.760 \pm 0.180) \times 10^3$ K and $n_e = (1.354 \pm 0.121) \times 10^4$ cm^{-3} for HH 204 and $n_e = (1.743 \pm 0.236) \times 10^4$ cm^{-3} for HH 202S. No adopted temperature is quoted for the latter, but our average value compares well with their $T_e([\mathrm{S\,II}]) = (8.25 \pm 0.54) \times 10^3$ K, $T_e([\mathrm{Ar\,III}]) = (8.26 \pm 0.41) \times 10^3$ K, and $T_e(\mathrm{He\,I}) = (7.95 \pm 0.20) \times 10^3$ K.

Table 5. Temperature and density fits of the [Fe III] observed spectra in HH 202S and HH 204 with the improved or new radiative (`atom`) and collisional (`coll`) datasets.

Datasets		HH 202S			HH 204		
Atom	**Coll**	$T_e(10^3\,\mathrm{K})$	$n_e(10^4\,\mathrm{cm}^{-3})$	χ^2	$T_e(10^3\,\mathrm{K})$	$n_e(10^4\,\mathrm{cm}^{-3})$	χ^2
BBQ10_34	BBQ10_34	7.68	1.94	6.31	9.49	1.51	47.6
BB14_34	BBQ10_34	8.24	1.80	3.84	9.91	1.44	28.1
DH09_34	BBQ10_34	7.94	1.31	2.24	9.25	0.82	21.8
Q96_34	BBQ10_34	7.97	1.66	3.54	9.39	1.19	35.6
BBQ10_34	BB14_34	7.83	2.17	5.57	9.01	2.16	50.0
BB14_34	BB14_34	8.47	2.14	4.56	9.03	1.49	33.2
DH09_34	BB14_34	8.18	1.78	3.23	9.00	1.16	9.95
Q96_34	BB14_34	8.12	1.91	3.97	8.97	1.49	11.9
BBQ10_34	Z96_34	7.34	2.51	1.74	8.53	1.71	16.9
BB14_34	Z96_34	7.94	2.32	2.54	8.23	1.61	28.5
DH09_34	Z96_34	7.71	1.97	0.68	8.34	1.30	4.36
Q96_34	Z96_34	7.68	2.24	1.00	8.11	1.73	4.62
BB14_144	BB14_144	8.47	2.12	4.57	9.03	1.49	33.2
BB14_144	Z96_144	7.94	2.33	2.54	8.24	1.61	28.5

3.3.3. Line-Ratio Diagnostics

Line-ratio diagnostics are widely used in nebular astrophysics to determine the plasma thermodynamic properties (temperature, density, and ionic abundances). They are based on the assumption that the observed line-intensity ratio is equivalent to the theoretical emissivity ratio

$$\frac{I(j,i)}{I(j,i')} = \frac{\epsilon(j,i)}{\epsilon(j,i')}\,. \tag{3}$$

Using our benchmarked atomic datasets for [Fe III], we investigate the impact of the atomic data scatter on the line-ratio temperature and density behaviors.

A common [Fe III] emissivity ratio to determine the plasma density in the range $3 \leq \log n_e \leq 6$ is $I(\lambda 4658)/I(\lambda 4702)$ (see, for instance, [10,11]). In Figure 1, we show its dependency on the atomic data. In the left panel, we select dataset atom_DH09_34 and plot $I(\lambda 4658)/I(\lambda 4702)$ as a function of density for three `coll` datasets: BBQ10_34, BB14_34, and Z96_34. Large discrepancies are found in the low-density regime ($\log n_e < 4$), particularly in coll_BBQ10_34 (40% lower than coll_Z96_34 at $\log n_e < 3$). In the right panel, we select dataset coll_Z96_34 and plot the emissivity ratio for four `atom` datasets: DH09_34, BBQ10_34, BB14_34, and Q96_34. Differences are not as large, atom_BBQ10_34 being the more discordant ($\sim$ 15% lower at $\log n_e < 3$).

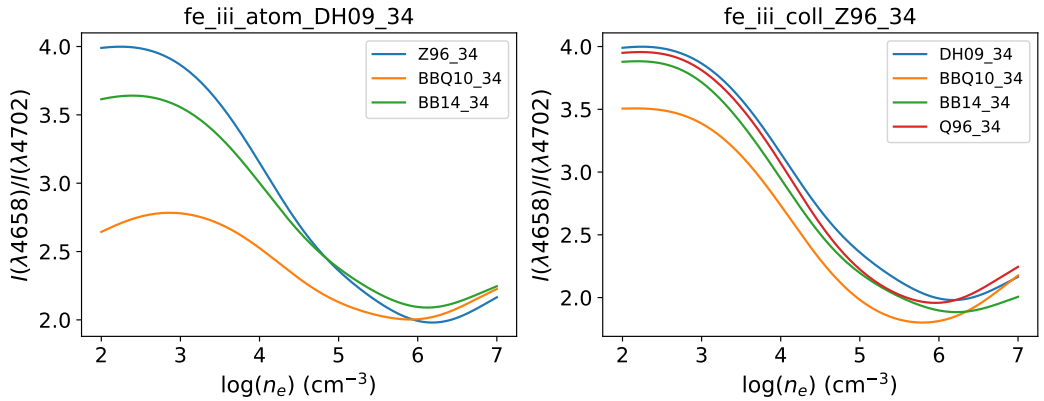

Figure 1. Density behavior of the [Fe III] $I(\lambda4658)/I(\lambda4702)$ emissivity ratio at $T_e = 7.9 \times 10^3$ K for different atomic datasets. **Left panel**: atom_DH09_34 dataset with three `coll` datasets (Z96_34, BBQ10_34, and BB14_34). **Right panel**: coll_Z96_34 dataset with four `atom` datasets (DH09_34, BBQ10_34, BB14_34, and Q96_34).

For $\log n_e \leq 3$, the emissivity ratio $I(\lambda4658)/I(\lambda4702)$ is practically density insensitive, being mostly dependent on the ECS of the involved atomic levels. To discern a reliable magnitude in this regime in the light of the discrepancies due to the collisional datasets, we select from the DESIRED database (Méndez-Delgado et al., unpublished) the following low-density sources: 30 Doradus [60]; Sh 2-311 [61]; M20 [62]; M17 [63]; HII-1, HII-2, UV-1 [64]; K932, NGC 5461, NGC 604, NGC 2363, NGC 4861, NGC 1741-C, NGC 5447, VS44, H1013 [65]; NGC 3125, POX 4, TOL 1924-416, TOL 1457-262, NGC 6822 (HV), NGC 5408 [66]; Sh 2-100, Sh 2-288 [67]; NGC 5471, NGC 5455 [68], Sh 2-152 [69]; and N44C, N11B, N66A, NGC 1714, IC 2111, N81 [70]. We then plot the observed line-intensity ratios in Figure 2 as a function of the [S II] density. In spite of the scatter, there is a definite trend for $I(\lambda4658)/I(\lambda4702) > 3.5$, which would reinforce the validity of the coll_BB14_34 and coll_Z96_34 datasets.

Regarding a useful [Fe III] temperature diagnostic, we choose $I(\lambda4658)/I(\lambda3240)$ due to its small variations in density and atomic data. In Figure 3, we plot this emissivity ratio as a function of temperature for the same `atom–coll` grid used in the density diagnostic. The curves show only a weak dependency on the choice of the collisional and radiative datasets.

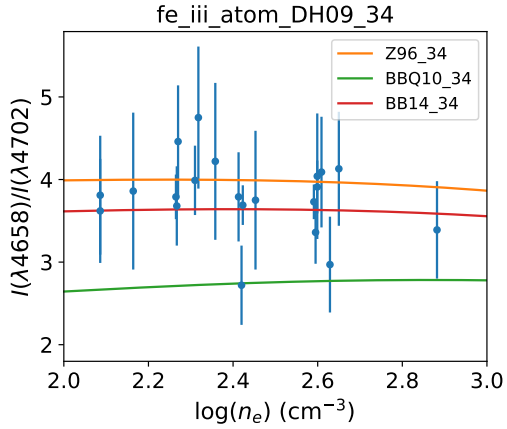

Figure 2. Observed [Fe III] $I(\lambda4658)/I(\lambda4702)$ line-intensity ratio from several low-density sources as a function of the [S II] density. The theoretical emissivity ratios determined by `PyNeb` with dataset atom_DH09_34 and three `coll` datasets (BBQ10_34, BB14_34, and Z96_34) are also depicted.

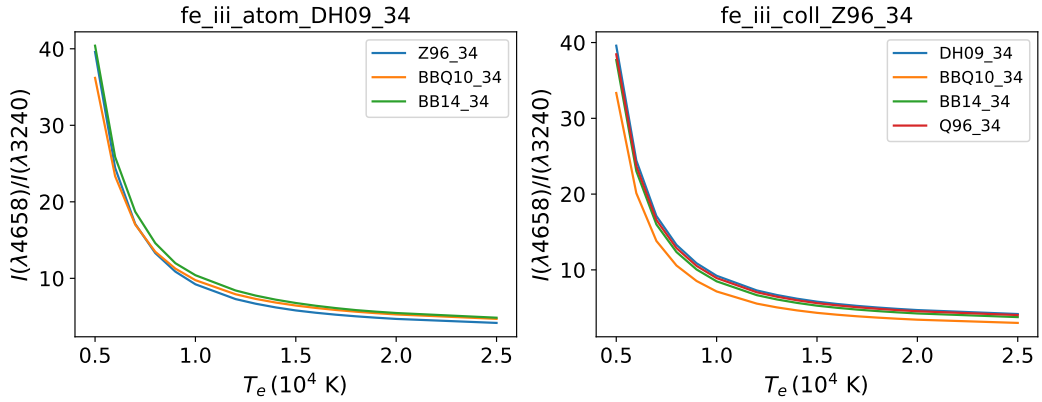

Figure 3. Temperature behavior of the [Fe III] $I(\lambda4658)/I(\lambda3240)$ emissivity ratio at $n_e = 2.1 \times 10^4\,\mathrm{cm}^{-3}$ for different atomic datasets. **Left panel**: dataset atom_DH09_34 with three `coll` datasets (Z96_34, BBQ10_34, and BB14_34). **Right panel**: dataset coll_Z96_34 with four `atom` datasets (DH09_34, BBQ10_34, BB14_34, and Q96_34).

A relevant question is whether the density and temperature estimates obtained from the $I(\lambda4658)/I(\lambda4702)$ and $I(\lambda4658)/I(\lambda3240)$ line ratios, respectively, compare with those obtained from the spectral fits described in Section 3.3.2. For HH 202S, as an example, the observed $I(\lambda4658)/I(\lambda4702) = 2.81$ and $I(\lambda4658)/I(\lambda3240) = 13.6$. In the density diagnostic, we set the temperature at $T_e = 7.9 \times 10^3$ K and obtain $n_e = 2.34 \times 10^4\,\mathrm{cm}^{-3}$ for the pair atom_DH09_34–coll_Z96_34 and $n_e = 1.86 \times 10^4\,\mathrm{cm}^{-3}$ for atom_DH09_34–coll_BB14_34, values that are fairly close to those obtained from the fits, respectively $n_e = 1.97 \times 10^4\,\mathrm{cm}^{-3}$ and $n_e = 1.78 \times 10^4\,\mathrm{cm}^{-3}$. However, if we designate the pair atom_DH09_34–coll_BBQ10_34, the theoretical $I(\lambda4658)/I(\lambda4702) < 2.78$ impairs a density reading for HH 202S. Furthermore, if we set the density at $n_e = 2.1 \times 10^4\,\mathrm{cm}^{-3}$, we obtain from the temperature diagnostic 7.89×10^3 K, 7.95×10^3 K, and 8.33×10^3 K for the `atom–coll` pairs DH09_34–Z96_34, DH09_34–BBQ10_34, and DH09_34–BB14_34, respectively, which compare well with 7.71×10^3 K, 7.94×10^3 K, and 8.18×10^3 K from the spectral fits.

3.4. Radiative Lifetimes of $3d^6$ *and* $3d^54s$ *Levels*

As previously mentioned, the [Fe III] nebular spectrum displays transitions between levels of the $3d^6$ and $3d^54s$ configurations. The `PyNeb` Fe III atomic models are based on the lower 34 levels with $E < 60,000\ \mathrm{cm}^{-1}$; that is, the cut is imposed just before the onset of the $3d^54s$ level array. As a result, in the present lifetime analysis, we obviate the $3d^6\ b^1D_2$ level at 77,044.67 cm^{-1} and the unobserved $3d^6\ ^1S_0$ estimated theoretically at $E > 99,000\ \mathrm{cm}^{-1}$. From $3d^54s$, only the lowly lying $^7S_3$ and $^5S_2$ levels are taken into account.

Radiative lifetimes derived from the A-values in the `atom` datasets BB14_34, BBQ10_34, DH09_34, and Q96_34 are compared in Figure 4. For each level, we determine the lifetime differences of these four datasets with respect to the average value. Such differences are, in general, within 0.1 dex except for five levels in atom_BB14_34, nine in atom_BBQ10_34, and two in each atom_DH09_34 and atom_Q96_34. Notably large discrepancies (as large as ~ 0.8 dex) are found for the $3d^6\ ^3H_J$ levels, which would affect the physical conditions and Fe^{2+} abundance derived from the $\lambda\lambda$4881, 4987, 4924, 5032, 4986 line intensities. Furthermore, the $3d^6\ b\ ^3P_J$ levels in atom_BB14_34 and $3d^6\ a\ ^3P_2$ and $a\ ^1G_4$ in atom_BBQ10_34 have lifetimes almost 0.2 dex lower. Significant differences also stand out for the $3d^54s\ ^7S_3$ and $^5S_2$ levels between these two datasets. A reassuring outcome is the agreement between the atom_DH09_34 and atom_Q96_34 lifetimes: within 20% except for the problematic ^3H_J levels. Most of the conclusions from this comparison are in line with [27].

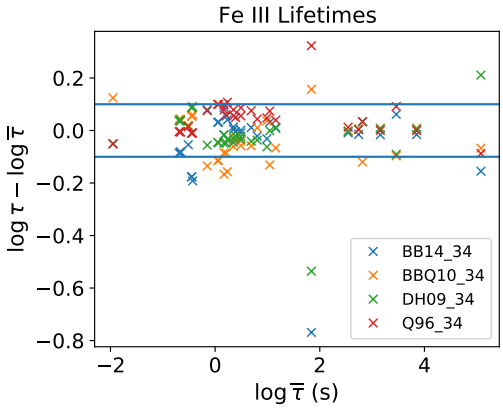

Figure 4. Comparison of Fe III radiative lifetimes computed from the A-values in the `atom` datasets BB14_34, BBQ10_34, DH09_34, and Q96_34 `atom` files. For each level, lifetime differences for these datasets with respect to the average value are plotted as a function of the average value.

3.5. Radiative Lifetimes of $3d^5 4p$ *Levels*

Apart from even-parity levels, dataset atom_BB14_144 contains 44 odd-parity levels belonging to the $3d^5 4p$ configuration. Their radiative lifetimes can be compared with those derived from the A-values computed with extensive CI (single and double excitations up to $n \leq 5$, $\ell \leq 3$, and 6p as well as selective promotions from the 3s and 3p subshells) with the MCBP code CIV3 [39]. As shown in Figure 5, the atom_BB14_144 lifetimes are on average 0.15 dex shorter. The larger differences are found for levels belonging to the $3d^5(^4P)4p\ ^3P^o$, $3d^5(^4P)4p\ ^5P^o$, and $3d^5(^4D)4p\ ^5F^o$ spectroscopic terms.

3.6. Effective Collision Strengths

As shown in Table 5, we have three revised `coll` datasets containing ECS for the 34-level atomic model of [Fe III]: Z96_34, BBQ10_34, and BB14_34. We compare these data at $T = 10^4$ K in Figure 6 using the latter as the reference. In general, there is a reasonable agreement for most transitions, but for several others, huge differences are encountered. Transitions involving the $3d^5(^6S)4s\ ^7S_3$ level are problematic. For instance, in Figure 6 (right panel), we have excluded from coll_Z96_34 transitions of the type $3d^5(^6S)4s\ ^7S_3 - 3d^6\ ^1L_J$ as they appear with $\Upsilon = 0.0$; furthermore, coll_Z96_34 transitions with $\Delta S = 3/2$ have abnormally small ECS ($\log \Upsilon < -4$). These shortcomings may be due to the non-relativistic method used in [25]. On the other hand, as discussed in [28], the main differences between the ECS in coll_BBQ10_34 and coll_BB14_34 are due to a mixup by the former in the assignments of the $3d^5(^6S)4s\ ^7S_3$ and $3d^6\ ^3G_3$ adjacent levels. Large discrepancies are also found in transitions of the type $3d^6$ a $^3P_J - 3d^6\ ^3H_{J'}$ and $3d^6$ b $^1G_4 - 3d^6\ ^5D_J$.

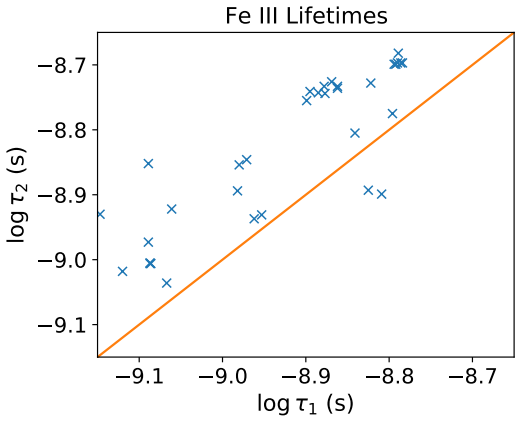

Figure 5. Comparison of radiative lifetimes for 44 levels of the $3d^5 4p$ configuration in Fe III derived from the A-values from atom_BB14_144 (τ_1) and Ref. [39] (τ_2).

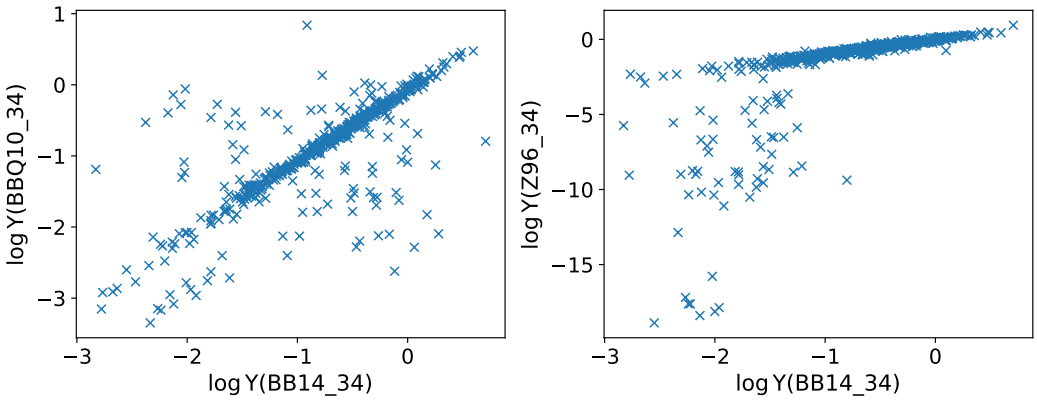

Figure 6. Comparison of [Fe III] ECS at $T = 10^4$ K in the coll_BBQ10_34 and coll_Z96_34 datasets with respect to those in coll_BB14_34.

3.7. Fe III Discussion

Our initial step in the present atomic data assessment was the comparison of observed line-intensity ratios with the corresponding theoretical A-value ratios for transitions arising from a common upper level (see Section 3.3.1). This procedure readily yields a first exposure of observational line misidentifications, blending, and contamination (e.g., telluric or instrumental) and of inherent computational difficulties such as strong valence–core correlation, double-excitation couplings, and strong CI mixing. Therefore, the agreement between theoretical ratios, on the one hand, and between observed and theoretical ratios, on the other hand, are both revealing.

Although the spectra of HH 202S and HH 204 are of comparable quality, the reported observational errors of the former are on average larger (36%) than the latter (12%). Comparisons among theoretical A-value ratios and with the observed counterparts lead to an overall accuracy level for the theoretical ratios of around 20–30%, except for odd theoretical outliers pinpointed in Section 3.3.1 believed to be caused by the aforementioned computational difficulties.

The spectrum fits performed in Section 3.3.2 bring to the fore a frequent drawback in modeling codes: the error-prone mapping of radiative or collisional datasets onto an atomic model with different level numbering as illustrated with dataset coll_BB14 that led to file deprecation. The four revised `atom` datasets (BBQ10_34, BB14_34, DH09_34, Q96_34) and three `coll` datasets (BBQ10_34, BB14_34, Z96_34) appear to give comparable temperatures and densities within

error bands of 6% and 20%, respectively, which also match satisfactorily estimates obtained from [Fe III] line-ratio diagnostics such as $I(\lambda4658)/I(\lambda4702)$ and $I(\lambda4658)/I(\lambda3240)$ (see Section 3.3.3) and from alternative ionic diagnostics reported in [9,11]. However, the density-sensitive ratio $I(\lambda4658)/I(\lambda4702)$ computed with coll_BBQ10_34 does not match the ratios observed in low-density ($\log n_e \lesssim 3$) nebular sources (see Figure 2).

As shown in Section 3.4, radiative lifetimes for levels of the $3d^6$ and $3d^54s$ configurations computed with A-values from the BBQ10_34, BB14_34, DH09_34, and Q96_34 `atom` datasets agree to within ~ 0.1 dex except for $3d^6\ ^3H_J$ and $3d^54s\ ^7S_J$,$^5S_2$. However, the best agreement ($\sim 20\%$) is found between A-values from structure calculations, namely atom_DH09_34 and atom_Q96_34, rather than those associated with scattering targets. This may be due to the convergence and accuracy of the CI expansions implemented in each calculation type. In structure calculations of radiative lifetimes for transitions involving levels of the $3d^6$ and $3d^54s$ configurations in Fe III, for instance, there is no need to include odd-parity configurations, while in a Fe III scattering target, a reduced set of configurations of both parity types must be considered. A similar argument may be applied to the lifetimes of $3d^54p$ levels (see Section 3.5), where the atom_BB14_144 lifetimes are on average shorter than those from a lengthy MCBP structure calculation [39].

The main finding of the ECS comparison in Section 3.6 is the large discrepancies displayed by coll_Z96_34 ECS with respect to coll_BB14_34 for some transitions with $\log \Upsilon < -1$ (see Figure 6), which may be due to the non-relativistic R-matrix method used by [25] in the computation of the former dataset. The larger ECS differences between coll_BBQ10_34 and coll_BB14_34 are mainly due to level misassignments.

Analyzing results from these data comparisons and spectral fits, we select as the [Fe III] default datasets in `PyNeb` 1.1.17 the atom_BB14_144 and coll_BB14_144 files, while files coll_BBQ10 and coll_BB14 are deprecated. Deprecated files are still available with the command `pn.atomicData.includeDeprecatedPath()`. Files atom_BBQ10 and coll_Z96 remain active, and files coll_BBQ10_34, atom_BB14_144, atom_DH09_34, and atom_Q96_34 are incorporated.

4. Fe II

Similarly to the Fe III atomic data assessment, we implement observational benchmarks to evaluate the atomic datasets for Fe II available in `PyNeb` 1.1.16, transcribing them directly from the source and implementing new models. NIST energy levels in this version of `PyNeb` are the same as those listed in the database of July 2022 [55].

4.1. Fe II Atomic Datasets in PyNeb

The following datasets are available for Fe II in `PyNeb` 1.1.16:

atom_VVKFHF99, coll_VVKFHF99 —These datasets list radiative and collisional rates for transitions among 80 levels with energies $E < 44,760\,\mathrm{cm}^{-1}$ compiled from different sources [71]. A-values for the dipole allowed and forbidden transitions are from [21] and [23], respectively. ECS are mainly from [24]; however, the source data are not available and A-values and ECS for transitions with spin change $\Delta S = 2$ have been obviated.

atom_B15, coll_B15 —A-values and ECS for transitions among 52 levels belonging to the $3d^7$, $3d^64s$, and $3d^54s^2$ configurations ($E < 31,500\,\mathrm{cm}^{-1}$) [29]. A-values were computed with the MCBP atomic structure code AUTOSTRUCTURE using different expansions and orbital optimization strategies and a dipole correction to the Thomas–Fermi–Dirac–Amaldi potential. Fine-tuning was carried out by means of term-energy corrections adjusted by fitting to the experimental term energies. ECS were computed with the Dirac–Coulomb R-matrix package DARC [34] using a target generated with the fully relativistic atomic structure code GRASP0 [54] using a six-configuration expansion comprising 329 levels.

atom_SRKFB19, coll_SRKFB19 —A-values and ECS for 250 levels from the $3d^7$, $3d^64s$, $3d^54s^2$, $3d^64p$, and $3d^54s4p$ configurations [31]. A-values were computed with GRASP0 in a 20-configuration expansion and ECS with DARC using a 716-level target representation.

4.2. Fe II *Revised and New Atomic Datasets*

For comparison purposes, models were normalized to 52 levels ($E < 31,500\,\mathrm{cm}^{-1}$), i.e., the number of levels considered in atom_B15 that includes the last even quartet term before the appearance of the $3d^64p$ level array. Two datasets have been extended to comprise 173 levels ($E < 66,100\,\mathrm{cm}^{-1}$), a cut before the onset of unmeasured levels in the NIST level list, and 225 levels ($E < 73,800\,\mathrm{cm}^{-1}$) to discuss some assignment inconsistencies. Although ECS from [24] are included in VVKFHF99, we have not considered their dataset individually as it excludes the doublet terms in their atomic model.

atom_QDZa96, atom_QDZh96 —E2 and M1 A-values calculated for transitions among the 63 levels of the configurations $3d^64s$, $3d^7$, and $3d^54s^2$ [23]. Extensive CI expansion was used with the Breit–Pauli SUPERSTRUCTURE [18] (QDZa96) and Pauli HFR [20] (QDZh96) atomic structure codes. These datasets are not complete enough to be used in `PyNeb` spectral modeling as they obviate transitions such as a $^4\mathrm{F} - \mathrm{a}\,^6\mathrm{D}$ and a $^2\mathrm{P} - \mathrm{a}\,^6\mathrm{D}$; therefore, they will only be used in radiative data comparisons.

atom_VVKFHF99_52, coll_VVKFHF99_52 —The VVKFHF99 datasets containing A-values and ECS described in Section 4.1 are reduced to 52 levels from even-parity configurations.

atom_DH11_52 —E2 and M1 A-values for transitions between levels of the $3d^64s$, $3d^7$, and $3d^54s^2$ configurations were computed in a large-scale CI framework with the MCBP structure code CIV3 [42]. Wave functions were fine-tuned to fit the experimental energies.

atom_B15_52, coll_B15_52 —Data (A-values and ECS) from the B15 calculation described in Section 4.1 were downloaded directly from the CDS, and the datasets were reconstructed.

atom_TZ18_52, coll_TZ18_52 —A-values and ECS were computed with the close-coupling B-spline Breit–Pauli R-matrix method for 340 levels of the $3d^64s$, $3d^7$, $3d^54s^2$, $3d^64p$, and $3d^54s4p$ configurations [30]. The CI target representation was constructed with a Hartree–Fock method. Semi-empirical fine-tuning in the structure and scattering calculations was introduced by fitting tothe experimental energies. The final Hamiltonian of the scattering calculation contains the spin–orbit term.

atom_SRKFB19_52, coll_SRKFB19_52 —Radiative and collisional data from the SRKFB19 calculation were described in Section 4.1. New files were constructed with data extracted from the `adf04_DARC716_2.10.18` file (Cathy Ramsbottom, private communication) and reduced to 52 levels.

atom_SRKFB19_173, coll_SRKFB19_173, atom_TZ18_173, coll_TZ18_173 —The SRKFB19 and TZ18 datasets have been extended to 173 levels ($E < 66,100\,\mathrm{cm}^{-1}$) to test model convergence.

atom_SRKFB19_225, atom_TZ18_225 —The theoretical SRKFB19 and TZ18 datasets have been extended to 225 levels ($E < 73,800\,\mathrm{cm}^{-1}$) to bring out term assignment inconsistencies involving levels with total orbital angular momentum quantum number $L = 5$ (see Table 6). With respect to NIST and other theoretical datasets, the term assignments of levels at 21,430.36 and 21,581.62 cm^{-1} ($\mathrm{a}\,^4\mathrm{H}$) and 26,170.18 and 26,352.77 cm^{-1} ($\mathrm{b}\,^2\mathrm{H}$) have been interchanged in atom_SRKFB19_225. Since the total angular momentum quantum number J of each level coincides in the different datasets, the incongruent term labeling would be inconsequential if the A-values for the transitions involving these levels were comparable. As shown in Table 7, this is not the case, as discrepancies as large as an order of magnitude were encountered. A similar mixup was found with the odd-parity $\mathrm{z}\,^4\mathrm{H^o}$ and $\mathrm{y}\,^2\mathrm{H^o}$ levels, which in this case are

even energetically misplaced (see Table 6). Assignment discrepancies of this sort could be due to strong CI admixture in terms with high orbital angular momentum ($L > 4$ say) in lowly ionized systems that the GRASP0 multi-configuration Dirac–Hartree–Fock structure code has problems resolving.

Table 6. Comparison of NIST energies (cm^{-1}) for levels in Fe II displaying a total orbital angular momentum quantum number $L = 5$ with those listed in different `atom` datasets (see Section 4.2). Questionable level assignments are found in atom_SRKFB19_225.

Level	NIST	SRKFB19_225	TZ18_225	DH11_52	B15_52	QDZh96
$3d^7\ a\ ^2H_{11/2}$	20,340.25	20,340.25	20,327.91	20,340.30	20,340.30	20,340
$3d^7\ a\ ^2H_{9/2}$	20,805.76	20,805.76	20,824.99	20,805.77	20,805.77	20,806
$3d^6(^3H)4s\ a\ ^4H_{13/2}$	21,251.58	21,251.58	21,283.52	21,251.61	21,251.61	21,252
$3d^6(^3H)4s\ a\ ^4H_{11/2}$	21,430.36	26,170.17	21,433.70	21,430.36	21,430.36	21,430
$3d^6(^3H)4s\ a\ ^4H_{9/2}$	21,581.62	26,352.77	21,560.17	21,581.64	21,581.64	21,582
$3d^6(^3H)4s\ a\ ^4H_{7/2}$	21,711.90	21,711.90	21,671.63	21,711.92	21,711.92	21,712
$3d^6(^3H)4s\ b\ ^2H_{11/2}$	26,170.18	21,430.36	26,186.48	26,170.18	26,170.18	26,170
$3d^6(^3H)4s\ b\ ^2H_{9/2}$	26,352.77	21,581.61	26,331.50	26,352.77	26,352.77	26,353
$3d^6(^3H)4p\ z\ ^4H^o_{13/2}$	60,837.56	60,837.55	60,832.43			
$3d^6(^3H)4p\ z\ ^4H^o_{11/2}$	60,887.61		60,880.58			
$3d^6(^3H)4p\ z\ ^4H^o_{9/2}$	60,989.44		61,012.21			
$3d^6(^3H)4p\ z\ ^4H^o_{7/2}$	61,156.83	61,156.82	61,178.84			
$3d^6(^3H)4p\ z\ ^2H^o_{11/2}$	65,363.61	65,363.60	65,333.65			
$3d^6(^3H)4p\ z\ ^2H^o_{9/2}$	65,556.27	65,556.26	65,551.82			
$3d^6(^3G)4p\ y\ ^4H^o_{13/2}$	66,411.71	66,411.70	66,306.76			
$3d^6(^3G)4p\ y\ ^4H^o_{11/2}$	66,463.54	66,463.54	66,602.84			
$3d^6(^3G)4p\ y\ ^4H^o_{9/2}$	66,589.04	66,589.03	66,733.10			
$3d^6(^3G)4p\ y\ ^4H^o_{7/2}$	66,672.34	66,672.32	66,705.11			
$3d^6(^3G)4p\ y\ ^2H^o_{11/2}$	67,516.33	67,516.32	67,942.69			
$3d^6(^3G)4p\ y\ ^2H^o_{11/2}$		67,709.96				
$3d^6(^3G)4p\ y\ ^2H^o_{9/2}$	68,000.79	68,000.77	67,609.99			
$3d^6(^3G)4p\ y\ ^2H^o_{9/2}$		68,201.16				
$3d^6(^1G2)4p\ x\ ^2H^o_{9/2}$	72,130.38	72,130.36	72,407.94			
$3d^6(^1G2)4p\ x\ ^2H^o_{11/2}$	72,261.74	72,261.73	71,962.96			
$3d^6(^1I)4p\ w\ ^2H^o_{11/2}$	73,603.54	73,603.53	73,435.97			
$3d^6(^1I)4p\ w\ ^2H^o_{9/2}$	73,751.28	73,751.27	73,868.28			

Table 7. *A*-values for transitions arising from the $3d^6 4s\,a\,^4H_J$ and $3d^6 4s\,b\,^2H_J$ levels ($J = 9/2$ and $11/2$) upper levels of [Fe II] listed in different `atom` datasets, which show the large discrepancies in atom_SRKFB19_225.

λ_{air} (Å)	*A*-Value (s^{-1})					
	SRKFB19_225	**TZ18_225**	**DH11_52**	**B15_52**	**QDZa96**	**QDZh96**
4114.48	1.52×10^{-2}	1.44×10^{-1}	1.61×10^{-1}	1.05×10^{-1}	7.80×10^{-2}	1.03×10^{-1}
4178.96	7.45×10^{-4}	3.26×10^{-2}	2.02×10^{-2}	1.89×10^{-2}	9.95×10^{-3}	1.56×10^{-2}
4211.11	1.81×10^{-2}	5.40×10^{-2}	5.93×10^{-2}	3.15×10^{-2}	3.37×10^{-2}	4.44×10^{-2}
4251.45	6.12×10^{-3}	2.86×10^{-2}	1.96×10^{-2}	1.33×10^{-2}	1.28×10^{-2}	1.87×10^{-2}
5111.64	4.68×10^{-1}	1.01×10^{-1}	1.07×10^{-1}	1.19×10^{-1}	1.20×10^{-1}	1.31×10^{-1}
5220.08	8.90×10^{-2}	1.09×10^{-1}	1.11×10^{-1}	1.32×10^{-1}	1.34×10^{-1}	1.44×10^{-1}
5261.63	$1.62 \times 10^{+0}$	3.25×10^{-1}	3.39×10^{-1}	3.95×10^{-1}	4.01×10^{-1}	4.29×10^{-1}
5333.66	8.85×10^{-1}	2.68×10^{-1}	2.78×10^{-1}	3.23×10^{-1}	3.32×10^{-1}	3.51×10^{-1}

4.3. Observational and Spectroscopic Benchmarks

Due to the wide astrophysical interest in Fe II, this ion presents interesting possibilities for implementing observational and spectroscopic benchmarks. There is interest not only in the forbidden-line spectrum but also in the allowed transition arrays involving levels from the odd-parity configurations $3d^6 4p$ and $3d^5 4s4p$, which may be populated by fluorescence pumping from the stellar continuum [72–74]. Fe II ultraviolet emission in active galactic nuclei is not fully understood, impeding quasar classification schemes and Fe abundance estimates [75].

4.3.1. *A*-Value Ratio Benchmark

In Tables 8 and 9, we compare the observed line-intensity ratios in the spectra of HH 202S and HH 204 involving transitions from a common upper level with the corresponding *A*-value ratios (see Equation (1)) from `atom` datasets B15_52, DH11_52, TZ18_52, SRKFB19_52, QDZa96, and QDZh96. In this comparison, we must point out the worrisome discrepancies displayed by some *A*-value ratios from atom_SRKFB19_52 with both the observed and other theoretical values; thus, the integrity of this radiative dataset is questionable.

Table 8. Comparison of [Fe II] line-intensity ratios for transitions arising from a common upper level in the HH 202S spectrum (Obs) with those estimated from *A*-values in the following `atom` datasets: B15_52 (T1); DH11_52 (T2); TZ18_52 (T3); SRKFB19_52 (T4); QDZa96 (T5); QDZh96 (T6). The error of the least significant figure of the observed intensity ratio is indicated in brackets.

Line 1			Line 2		Obs	T1	T2	T3	T4	T5	T6
Upper	Lower	λ_{air}(Å)	Lower	λ_{air}(Å)	Line Intensity Ratio						
b $^2H_{9/2}$	a $^4F_{7/2}$	4178.96	a $^4F_{5/2}$	4251.45	1.3(9)	1.44	1.05	1.16	0.12	0.79	0.85
b $^2H_{11/2}$	a $^4F_{9/2}$	4114.48	a $^4F_{7/2}$	4211.11	2.4(8)	3.42	2.78	2.73	0.86	2.37	2.37
a $^4G_{7/2}$	a $^4F_{5/2}$	4319.62	a $^4F_{3/2}$	4372.43	2.4(8)	2.00	1.95	1.97	1.88	1.98	1.96
a $^4G_{9/2}$	a $^4F_{9/2}$	4177.20	a $^4F_{7/2}$	4276.84	0.28(8)	0.24	0.21	0.23	0.29	0.25	0.24
a $^4G_{9/2}$	a $^4F_{7/2}$	4276.84	a $^4F_{5/2}$	4352.78	2.1(6)	2.16	2.15	2.24	2.07	2.21	2.19
a $^4G_{11/2}$	a $^4F_{9/2}$	4243.97	a $^4F_{7/2}$	4346.86	5(1)	4.40	4.54	4.67	4.24	4.60	4.59
a $^6S_{5/2}$	a $^6D_{9/2}$	4287.39	a $^6D_{7/2}$	4359.33	1.3(3)	1.37	1.37	1.38	1.35	1.37	1.38
a $^6S_{5/2}$	a $^6D_{7/2}$	4359.33	a $^6D_{5/2}$	4413.78	1.4(3)	1.44	1.43	1.44	1.42	1.42	1.44
a $^6S_{5/2}$	a $^6D_{5/2}$	4413.78	a $^6D_{3/2}$	4452.10	1.6(4)	1.58	1.57	1.58	1.56	1.57	1.58
a $^6S_{5/2}$	a $^6D_{3/2}$	4452.10	a $^6D_{1/2}$	4474.90	2.2(7)	2.07	2.06	2.06	2.05	2.06	2.06
b $^4F_{3/2}$	a $^6D_{3/2}$	4509.61	a $^4F_{5/2}$	4950.76	0.4(2)	0.31	0.40	0.38	0.11	0.28	0.28
b $^4F_{3/2}$	a $^4F_{5/2}$	4950.76	a $^4F_{3/2}$	5020.24	0.9(4)	0.96	0.97	0.98	0.95	0.97	0.97
b $^4F_{5/2}$	a $^6D_{7/2}$	4432.45	a $^6D_{5/2}$	4488.75	0.6(3)	0.36	0.36	0.36	0.36	0.37	0.36
b $^4F_{5/2}$	a $^6D_{5/2}$	4488.75	a $^6D_{3/2}$	4528.38	3(2)	3.44	3.44	3.43	3.38	3.42	3.45
b $^4F_{5/2}$	a $^6D_{3/2}$	4528.38	a $^4F_{7/2}$	4874.50	0.3(2)	0.23	0.30	0.28	0.09	0.22	0.21
b $^4F_{5/2}$	a $^4F_{7/2}$	4874.50	a $^4F_{5/2}$	4973.40	1.3(5)	1.25	1.24	1.27	1.26	1.26	1.24
b $^4F_{5/2}$	a $^4F_{5/2}$	4973.40	a $^4F_{3/2}$	5043.53	1.5(7)	2.01	2.07	1.99	1.61	1.93	1.97
b $^4F_{7/2}$	a $^6D_{7/2}$	4457.95	a $^6D_{5/2}$	4514.90	4(2)	4.30	4.35	4.32	4.22	4.30	4.34
b $^4F_{7/2}$	a $^6D_{5/2}$	4514.90	a $^4F_{9/2}$	4774.73	0.6(3)	0.46	0.60	0.56	0.19	0.44	0.42
b $^4F_{7/2}$	a $^4F_{9/2}$	4774.73	a $^4F_{7/2}$	4905.35	0.6(2)	0.58	0.58	0.60	0.72	0.59	0.59
b $^4F_{9/2}$	a $^6D_{9/2}$	4416.27	a $^6D_{7/2}$	4492.64	7(2)	7.61	7.54	7.70	7.41	7.60	7.74
b $^4F_{9/2}$	a $^6D_{7/2}$	4492.64	a $^4F_{9/2}$	4814.54	0.15(5)	0.14	0.19	0.17	0.07	0.13	0.12
b $^4F_{9/2}$	a $^4F_{9/2}$	4814.54	a $^4F_{7/2}$	4947.39	7(2)	7.57	6.35	7.00	0.88	7.09	7.17
b $^4F_{9/2}$	a $^4F_{7/2}$	4947.39	a $^4D_{7/2}$	6809.24	4(2)	3.49	3.22	3.07	70.2	3.98	4.16
b $^4P_{3/2}$	a $^6D_{5/2}$	4728.07	a $^4F_{7/2}$	5158.01	0.9(3)	1.23	1.83	2.00	0.57	1.29	1.19
b $^4P_{3/2}$	a $^4F_{7/2}$	5158.01	a $^4F_{5/2}$	5268.89	3(1)	1.57	1.56	1.57	1.48	1.57	1.56
a $^4H_{7/2}$	a $^4F_{5/2}$	5296.84	a $^4F_{3/2}$	5376.47	0.3(1)	0.32	0.34	0.34	0.13	0.34	0.34
a $^4H_{9/2}$	a $^4F_{7/2}$	5220.08	a $^4F_{5/2}$	5333.66	0.4(1)	0.42	0.41	0.42	0.10	0.41	0.42
a $^4H_{11/2}$	a $^4F_{9/2}$	5111.64	a $^4F_{7/2}$	5261.63	0.32(6)	0.31	0.32	0.32	0.30	0.31	0.31
a $^2D2_{3/2}$	a $^6D_{3/2}$	4889.71	a $^4F_{5/2}$	5412.68	3(1)	0.00	0.00	0.00	0.00	0.00	0.00
a $^2D2_{3/2}$	a $^4F_{5/2}$	5412.68	a $^4F_{3/2}$	5495.84	2(1)	1.89	1.91	1.90	1.89	1.89	1.90
b $^4P_{5/2}$	a $^4F_{9/2}$	5273.36	a $^4F_{7/2}$	5433.15	3(1)	3.32	2.88	3.19	3.27	3.28	3.26
a $^2D2_{5/2}$	a $^4F_{7/2}$	5527.35	a $^4F_{5/2}$	5654.87	10(4)	9.26	9.09	9.19	9.12	9.06	8.98
a $^2G_{7/2}$	a $^4F_{7/2}$	7172.00	a $^4F_{5/2}$	7388.17	1.4(3)	1.35	1.35	1.36	1.32	1.35	1.35
a $^2G_{9/2}$	a $^4F_{9/2}$	7155.17	a $^4F_{7/2}$	7452.56	3.1(5)	3.17	3.22	3.23	3.10	3.19	3.24
a $^4P_{1/2}$	a $^4F_{5/2}$	9033.49	a $^4F_{3/2}$	9267.55	0.8(2)	0.77	0.78	0.78	0.50	0.78	0.78
a $^4P_{3/2}$	a $^6D_{5/2}$	7686.93	a $^4F_{7/2}$	8891.93	0.27(7)	0.26	0.83	0.44	0.40	0.36	0.44
a $^4P_{3/2}$	a $^4F_{7/2}$	8891.93	a $^4F_{5/2}$	9226.63	1.7(3)	1.76	1.79	1.78	0.88	1.78	1.80
a $^4P_{5/2}$	a $^6D_{7/2}$	7637.52	a $^4F_{7/2}$	9051.95	0.5(1)	0.59	1.96	1.08	0.18	0.89	1.15
a $^4P_{5/2}$	a $^4F_{7/2}$	9051.95	a $^4F_{5/2}$	9399.04	7(2)	5.13	5.32	5.21	2.64	5.46	5.67

Table 9. Comparison of [Fe II] line-intensity ratios for transitions arising from a common upper level in the HH 204 spectrum (Obs) with those estimated from A-values in the following `atom` datasets: B15_52 (T1); DH11_52 (T2); TZ18_52 (T3); SRKFB19_52 (T4); QDZa96 (T5); QDZh96 (T6). The error of the least significant figure of the observed intensity ratio is indicated in brackets.

Line 1			Line 2		Obs	T1	T2	T3	T4	T5	T6
Upper	Lower	λ_{air}(Å)	Lower	λ_{air}(Å)	Line Intensity Ratio						
a $^2F_{7/2}$	a $^4D_{7/2}$	5163.96	a $^2G_{9/2}$	8715.80	9(2)	7.50	10.5	11.1	2.81	6.73	7.48
b $^2H_{9/2}$	a $^4F_{7/2}$	4178.96	a $^4F_{5/2}$	4251.45	1.2(2)	1.44	1.05	1.16	0.12	0.79	0.85
b $^2H_{11/2}$	a $^4F_{9/2}$	4114.48	a $^4F_{7/2}$	4211.11	2.6(2)	3.42	2.78	2.73	0.86	2.37	2.37
a $^4G_{5/2}$	a $^6D_{3/2}$	3968.27	a $^4F_{5/2}$	4305.90	7(1)	0.00	0.00	0.00	0.00	0.00	0.00
a $^4G_{5/2}$	a $^4F_{5/2}$	4305.90	a $^4F_{3/2}$	4358.37	0.56(8)	0.44	0.42	0.44	0.48	0.46	0.45
a $^4G_{7/2}$	a $^4F_{5/2}$	4319.62	a $^4F_{3/2}$	4372.43	2.0(2)	2.00	1.95	1.97	1.88	1.98	1.96
a $^4G_{9/2}$	a $^4F_{9/2}$	4177.20	a $^4F_{7/2}$	4276.84	0.25(2)	0.24	0.21	0.23	0.29	0.25	0.24
a $^4G_{9/2}$	a $^4F_{7/2}$	4276.84	a $^4F_{5/2}$	4352.78	2.1(1)	2.16	2.15	2.24	2.07	2.21	2.19
a $^4G_{11/2}$	a $^4F_{9/2}$	4243.97	a $^4F_{7/2}$	4346.86	4.9(2)	4.40	4.54	4.67	4.24	4.60	4.59
a $^6S_{5/2}$	a $^6D_{9/2}$	4287.39	a $^6D_{7/2}$	4359.33	1.39(6)	1.37	1.37	1.38	1.35	1.37	1.38
a $^6S_{5/2}$	a $^6D_{7/2}$	4359.33	a $^6D_{5/2}$	4413.78	1.42(6)	1.44	1.43	1.44	1.42	1.42	1.44
a $^6S_{5/2}$	a $^6D_{5/2}$	4413.78	a $^6D_{3/2}$	4452.10	1.55(6)	1.58	1.57	1.58	1.57	1.57	1.58
a $^6S_{5/2}$	a $^6D_{3/2}$	4452.10	a $^6D_{1/2}$	4474.90	2.0(1)	2.07	2.06	2.06	2.05	2.06	2.06
b $^4F_{3/2}$	a $^6D_{3/2}$	4509.61	a $^4F_{5/2}$	4950.76	0.42(9)	0.31	0.40	0.38	0.11	0.28	0.28
b $^4F_{3/2}$	a $^4F_{5/2}$	4950.76	a $^4F_{3/2}$	5020.24	1.4(3)	0.96	0.97	0.98	0.95	0.97	0.97
b $^4F_{5/2}$	a $^6D_{7/2}$	4432.45	a $^6D_{5/2}$	4488.75	0.49(7)	0.36	0.36	0.36	0.36	0.37	0.36
b $^4F_{5/2}$	a $^6D_{5/2}$	4488.75	a $^6D_{3/2}$	4528.38	3.6(7)	3.44	3.44	3.43	3.38	3.42	3.45
b $^4F_{5/2}$	a $^6D_{3/2}$	4528.38	a $^4F_{7/2}$	4874.50	0.25(5)	0.23	0.30	0.28	0.09	0.22	0.21
b $^4F_{5/2}$	a $^4F_{7/2}$	4874.50	a $^4F_{5/2}$	4973.40	1.4(1)	1.25	1.24	1.27	1.26	1.26	1.24
b $^4F_{5/2}$	a $^4F_{5/2}$	4973.40	a $^4F_{3/2}$	5043.53	1.9(3)	2.01	2.07	1.99	1.61	1.93	1.97
b $^4F_{7/2}$	a $^6D_{9/2}$	4382.74	a $^6D_{7/2}$	4457.95	0.19(2)	0.20	0.21	0.20	0.20	0.21	0.20
b $^4F_{7/2}$	a $^6D_{7/2}$	4457.95	a $^6D_{5/2}$	4514.90	4.3(4)	4.30	4.35	4.32	4.22	4.30	4.34
b $^4F_{7/2}$	a $^6D_{5/2}$	4514.90	a $^4F_{9/2}$	4774.73	0.56(6)	0.46	0.60	0.56	0.19	0.44	0.42
b $^4F_{7/2}$	a $^4F_{9/2}$	4774.73	a $^4F_{7/2}$	4905.35	0.57(4)	0.58	0.58	0.60	0.72	0.59	0.59
b $^4F_{9/2}$	a $^6D_{9/2}$	4416.27	a $^6D_{7/2}$	4492.64	7.7(5)	7.61	7.54	7.70	7.41	7.60	7.74
b $^4F_{9/2}$	a $^6D_{7/2}$	4492.64	a $^4F_{9/2}$	4814.54	0.15(1)	0.14	0.19	0.17	0.07	0.13	0.12
b $^4F_{9/2}$	a $^4F_{9/2}$	4814.54	a $^4F_{7/2}$	4947.39	7.8(5)	7.57	6.35	7.00	0.88	7.09	7.17
b $^4F_{9/2}$	a $^4F_{7/2}$	4947.39	a $^4D_{7/2}$	6809.24	3.2(4)	3.49	3.22	3.07	70.21	3.98	4.16
b $^4P_{3/2}$	a $^6D_{5/2}$	4728.07	a $^4F_{5/2}$	5268.89	2.3(4)	1.93	2.85	3.14	0.84	2.02	1.85
a $^4H_{7/2}$	a $^4F_{5/2}$	5296.84	a $^4F_{3/2}$	5376.47	0.36(5)	0.32	0.34	0.34	0.13	0.34	0.34
a $^4H_{9/2}$	a $^4F_{7/2}$	5220.08	a $^4F_{5/2}$	5333.66	0.44(5)	0.42	0.41	0.42	0.10	0.41	0.42
a $^4H_{11/2}$	a $^4F_{9/2}$	5111.64	a $^4F_{7/2}$	5261.63	0.34(3)	0.31	0.32	0.32	0.30	0.31	0.31
a $^2D2_{3/2}$	a $^6D_{3/2}$	4889.71	a $^4F_{3/2}$	5495.84	12(2)	0.00	0.00	0.00	0.00	0.00	0.00
b $^4P_{5/2}$	a $^4F_{9/2}$	5273.36	a $^4F_{7/2}$	5433.15	2.7(2)	3.32	2.88	3.19	3.27	3.28	3.26
b $^4P_{5/2}$	a $^4F_{7/2}$	5433.15	a $^4D_{7/2}$	7764.71	7(1)	7.22	5.64	4.88	22.63	7.01	7.42
a $^2G_{7/2}$	a $^4F_{9/2}$	6896.17	a $^4F_{7/2}$	7172.00	0.10(1)	0.10	0.09	0.09	0.09	0.10	0.09
a $^2G_{7/2}$	a $^4F_{7/2}$	7172.00	a $^4F_{5/2}$	7388.17	1.34(9)	1.35	1.35	1.36	1.32	1.35	1.35
a $^2G_{9/2}$	a $^4F_{9/2}$	7155.17	a $^4F_{7/2}$	7452.56	3.2(2)	3.17	3.22	3.23	3.10	3.19	3.24
a $^4P_{1/2}$	a $^6D_{3/2}$	7665.28	a $^6D_{1/2}$	7733.13	2.8(7)	3.26	3.31	3.28	4.44	3.26	3.28
a $^4P_{1/2}$	a $^6D_{1/2}$	7733.13	a $^4F_{5/2}$	9033.49	0.11(2)	0.10	0.32	0.17	0.10	0.14	0.17
a $^4P_{1/2}$	a $^4F_{5/2}$	9033.49	a $^4F_{3/2}$	9267.55	0.75(7)	0.77	0.78	0.78	0.50	0.78	0.78
a $^4P_{3/2}$	a $^6D_{5/2}$	7686.93	a $^6D_{1/2}$	7874.23	7(1)	7.06	7.31	7.05	11.24		
a $^4P_{3/2}$	a $^6D_{1/2}$	7874.23	a $^4F_{7/2}$	8891.93	0.03(1)	0.04	0.11	0.06	0.04		
a $^4P_{3/2}$	a $^4F_{7/2}$	8891.93	a $^4F_{5/2}$	9226.63	1.7(2)	1.76	1.79	1.78	0.88	1.78	1.80
a $^4P_{5/2}$	a $^6D_{3/2}$	7926.88	a $^4F_{7/2}$	9051.95	0.05(1)	0.04	0.14	0.08	0.00		
a $^4P_{5/2}$	a $^4F_{7/2}$	9051.95	a $^4F_{5/2}$	9399.04	5.4(6)	5.13	5.32	5.21	2.64	5.46	5.67

For two cases, the observed line-intensity ratios are very different from the corresponding theoretical values: $I(\lambda 3968.27)/I(\lambda 4305.90)$ and $I(\lambda 4889.71)/I(\lambda 5412.68)$, which are caused by the misidentification of the stronger [Fe II] $\lambda\lambda$3968.66, 4889.62 lines with the weaker [Fe II] $\lambda\lambda$3968.27, 4889.71, which are emitted from different atomic transitions.

Excluding atom_SRKFB19_52, the A-value ratios in Tables 8 and 9 agree to $\sim 20-25\%$ except for two cases in HH 202S, $I(\lambda 7637.52)/I(\lambda 9051.95)$ and $I(\lambda 7686.93)/I(\lambda 8891.93)$, and one in HH 204, $I(\lambda 7733.13)/I(\lambda 9033.49)$, which are caused by lines with A-values of order $\lesssim 10^{-3}$ subject to large numerical uncertainties. Most theoretical ratios are within the estimated observational error bars except for those involving A-values strongly affected by level mixing effects that are frequent in Fe II [40].

4.3.2. [Fe II] Spectrum Fits

In a similar manner to [Fe III] (see Section 3.3.2), we fit the reliable [Fe II] lines of the high-resolution spectra of the bright objects HH 202S and HH 204 with `PyNeb` theoretical emissivities optimized through a least-square procedure in terms of the electron temperature and density. The theoretical emissivity and observed intensity of each line are, respectively, normalized to the sum of the emissivities and the sum of intensities.

In the spectrum fit of HH 202S and HH 204, a selection of lines were excluded mainly due to observational problems [9,11]: $\lambda\lambda$4413.78, 4416.27, 4452.10, 4509.61, 4514.90, 4528.38, 4889.71, and 4905.35 in addition to $\lambda\lambda$4276.84, 4319.62, 4359.33, 4452.10, 7665.28, 9399.04, and 9997.49 in the latter source. The line λ4382.74 is also questionable due to an incorrect identification.

We show in Table 10 the results of the spectral fits with the atomic datasets available in `PyNeb` 1.1.16. In contrast to [Fe III] (see Section 3.3.2), the optimization procedure does not always converge to the desired accuracy (e.g., SRKFB19 for HH 204), and the density variation may not show a minimum or may depend on the initial input value. The temperature scatter is worrisome, and the HH 204 fits, in particular, show large values of χ^2.

Table 10. Temperature and density fits of the [Fe II] observed spectra of HH 202S and HH 204 with the radiative (`atom`) and collisional (`coll`) datasets currently available in `PyNeb` 1.1.16.

Datasets		**HH 202S**			**HH 204**		
Atom	**Coll**	T_e **(10³ K)**	n_e **(10⁴ cm⁻³)**	χ^2	T_e **(10³ K)**	n_e **(10⁴ cm⁻³)**	χ^2
B15	B15	13.0	6.43	4.40	24.6	3.92	90.8
VVKFHF99	VVKFHF99	9.87	1.52	7.80	12.8	0.98	105.
SRKFB19	SRKFB19	18.8	2.67	19.6			

The revised and new Fe II atomic models comprise four radiative (`atom`) and four collisional (`coll`) files normalized to 52 levels. The spectral fits for HH 202S and HH 204 are shown in Table 11, where each collisional dataset appears to lead to a diverse temperature and density pair (T_e, n_e). For HH 202S in units of 10^3 K and 10^4 cm^{-3}, respectively,

coll_B15_52: $(12.0 \pm 0.1, 6.3 \pm 0.6)$

coll_TZ18_52: $(8.3 \pm 0.4, 3.9 \pm 0.5)$

coll_SRKFB19_52: $(10.3 \pm 0.6, 2.4 \pm 0.3)$

coll_VVKFHF99_52: $(10.2 \pm 0.7, 1.6 \pm 0.2)$

where the scatter in both temperature and density due to the atomic data is surprisingly broad, and only the temperature from coll_TZ18_52, $T_e = (8.3 \pm 0.4) \times 10^3$ K, agrees with that determined from the [Fe III] fit, $T_e = (7.9 \pm 0.3) \times 10^3$ K (see Section 3.3.2). On the other

Table 11. Temperature and density fits of the [Fe II] observed spectra in HH 202S and HH 204 with the improved and new radiative (`atom`) and collisional (`coll`) datasets.

Datasets		HH 202S			HH 204		
Atom	**Coll**	$T_e(10^3\,\mathrm{K})$	$n_e(10^4\,\mathrm{cm^{-3}})$	χ^2	$T_e(10^3\,\mathrm{K})$	$n_e(10^4\,\mathrm{cm^{-3}})$	χ^2
B15_52	B15_52	11.6	5.99	1.51	16.5	3.90	67.0
DH11_52	B15_52	13.4	6.00	4.60	22.7	4.00	94.7
TZ18_52	B15_52	11.4	5.98	1.94	17.1	3.69	70.1
VVKFHF99_52	B15_52	11.7	7.12	2.10	17.4	3.52	75.5
TZ18_52	TZ18_52	7.94	3.29	7.90	11.2	2.63	154.
B15_52	TZ18_52	8.14	4.10	7.37	11.5	3.62	145.
DH11_52	TZ18_52	8.92	3.95	9.06	13.1	3.02	160.
VVKFHF99_52	TZ18_52	8.09	4.43	7.37	11.8	3.95	147.
B15_52	SRKFB19_52	10.0	2.05	2.20	14.5	0.89	85.8
DH11_52	SRKFB19_52	11.1	2.58	4.77	17.3	0.89	96.3
TZ18_52	SRKFB19_52	9.91	2.21	2.75	15.2	1.15	84.7
VVKFHF99_52	SRKFB19_52	10.1	2.73	2.71	15.6	1.24	90.4
VVKFHF99_52	VVKFHF99_52	9.92	1.66	7.79	12.7	0.89	106.
B15_52	VVKFHF99_52	9.85	1.43	7.19	12.1	0.81	88.3
DH11_52	VVKFHF99_52	11.2	1.75	12.5	16.7	0.93	164.
TZ18_52	VVKFHF99_52	9.94	1.47	7.70	13.0	0.79	101.
TZ18_173	TZ18_173	7.81	3.29	7.91	10.4	1.51	40.2
TZ18_173	SRKFB19_173	9.75	2.32	2.84	15.5	1.19	64.2

hand, the density $n_e = (2.1 \pm 0.3) \times 10^4\,\mathrm{cm^{-3}}$ obtained in the [Fe III] fit matches the values by coll_SRKFB19_52, $(2.4 \pm 0.3) \times 10^4\,\mathrm{cm^{-3}}$, and coll_VVKFHF99_52, $(1.6 \pm 0.2) \times 10^4\,\mathrm{cm^{-3}}$.

For HH 204,

coll_B15_52: $(18.4 \pm 0.3, 3.8 \pm 0.2)$

coll_TZ18_52: $(11.9 \pm 0.1, 3.3 \pm 0.6)$

coll_SRKFB19_52: $(15.7 \pm 0.1, 1.0 \pm 0.2)$

coll_VVKFHF99_52: $(13.6 \pm 0.2, 0.85 \pm 0.07)$

whereby the temperatures are significantly higher than the [Fe III] value $T_e = (8.9 \pm 0.6) \times 10^3$ K, while the [Fe III] density, $n_e = (1.5 \pm 0.3) \times 10^4\,\mathrm{cm^{-3}}$, favors coll_SRKFB19_52.

This confusing situation may lead to different analyses. For instance, in Figure 7, we plot for lines in HH 202S the ratio of the normalized theoretical emissivity to the normalized observed intensity as a function of the upper-level energy of the transition. In the left panel, the spectrum was fitted with datasets on atom_TZ18_52 and coll_TZ18_52, resulting in the low-temperature $T_e = 7.94 \times 10^3$ K and density $n_e = 3.29 \times 10^4\,\mathrm{cm^{-3}}$. For transitions with upper-level energies $E < 2 \times 10^4\,\mathrm{cm^{-1}}$, the number of ratios above and below 1.0 is roughly equal, while at the higher energies, the number of ratios above 1.0 progressively diminishes. This behavior is similar to that depicted in Figure 4 of [73], interpreted as a signature of missing fluorescence pumping by the stellar continuum in the plasma model.

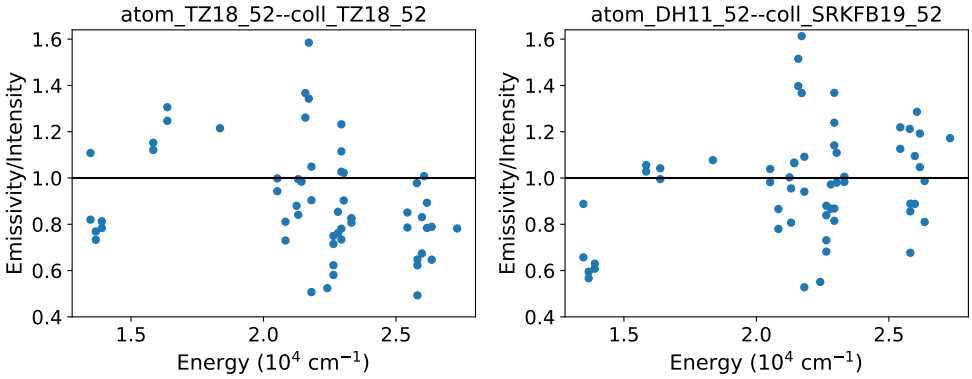

Figure 7. Ratio of the normalized theoretical emissivity and observed intensity for lines in HH 202S as a function of the upper-level energy of the transition. **Left panel**: spectral fit with datasets atom_TZ18_52 and coll_TZ18_52 at $T_e = 7.94 \times 10^3$ K and $n_e = 3.29 \times 10^4$ cm^{-3}. **Right panel**: spectral fit with datasets atom_DH11_52 and coll_SRKFB19_52 at $T_e = 11.1 \times 10^3$ K and $n_e = 2.58 \times 10^4$ cm^{-3}.

In the right panel, the spectral fit was performed with datasets atom_DH11_52 and coll_SRKFB19_52, resulting in a higher temperature $T_e = 11.1 \times 10^3$ K and comparable density $n_e = 2.58 \times 10^4$ cm^{-3}; however, the missing continuum-pumping signature is not present. The diverse, high temperatures of Table 11 might thus be interpreted as attempts to fit the spectra without accounting for all the level-populating mechanisms.

A second reading is to look at the critical densities of the levels. In Figure 8, we plot the critical densities at $T_e = 10^4$ K for the lower 52 levels of [Fe II] computed with dataset atom_TZ18_52 and three `coll` files: B15_52, SRKFB19_52, and TZ18_52. For levels with index $i > 10$, critical densities by coll_B15_52 are a factor of two higher, and for $i > 35$, they are all significantly different from each other. A key feature is the low critical density ($\log \rho_{\rm crit} < 2.6$) of the 3d^7 a ^{4}F$_{9/2}$ metastable level (level $i = 6$). For an electron density $n_e = 2 \times 10^4$ cm^{-3}, the population of this level may be larger than that of the ground level for temperatures as low as $T_e \approx 7 \times 10^3$ K; therefore, this level plays a dominant role in the spectral formation of [Fe II].

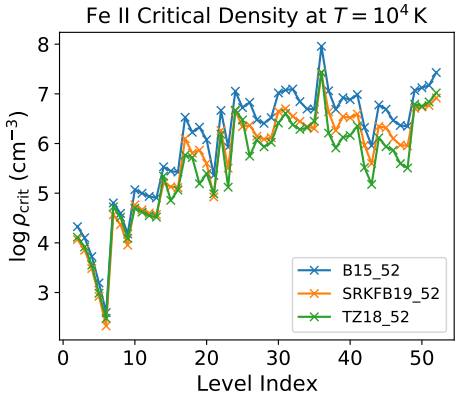

Figure 8. Critical densities for the lower 52 levels of [Fe II] predicted at $T = 10^4$ K by using ECS from the `coll` datasets B15_52, SRKFB19_52, and TZ18_52 and A-values from atom_TZ18_52.

Moreover, in Figure 9, we plot the critical density of level 3d^7 a ^{4}F$_{9/2}$ as a function of temperature using different atomic datasets. In the right panel, we show results computed with the dataset coll_TZ18_52 and three `atom` files (TZ18_52, B15_52, and DH11_52). Although the sensitivity to the radiative data is extreme, for $T_e > 5 \times 10^3$ K, it is approximately temperature

independent. In the left panel, the critical density is computed with the atom_TZ18_52 and three `coll` datasets (B15_52, SRKFB19_52, and TZ18_52). The dependency on the collisional data is not as marked as on the radiative data, but it is temperature dependent.

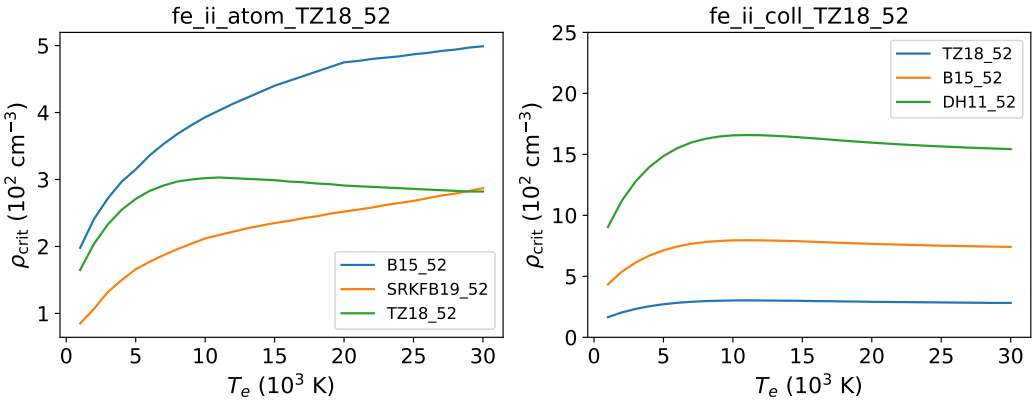

Figure 9. Critical density of level $3d^7\ a\ ^4F_{9/2}$ of [Fe II] as a function of temperature computed with different atomic datasets. **Left panel**: atom_TZ18_52 file and three `coll` files: B15_52, SRKFB19_52, and TZ18_52. **Right panel**: coll_TZ18_52 file and three `atom` files: TZ18_52, B15_52, and DH11_52.

In Table 11, we also list the fit results using the extended dataset pairs atom_TZ18_173–coll_TZ18_173 and atom_TZ18_173–coll_SRKFB19_173. For the HH 202S spectrum, the resulting temperature (in 10^3 K units), density (in 10^4 cm^{-3} units), and χ^2 values $(T_e, n_e, \chi^2) = (7.81, 3.29, 7.91)$ and $(T_e, n_e, \chi^2) = (9.75, 2.32, 2.84)$, respectively, are, as expected, close to those from the atom_TZ18_52–coll_TZ18_52 and atom_TZ18_52–coll_SRKFB19_52 pairs: $(T_e, n_e, \chi^2) = (7.94, 3.29, 7.90)$ and $(T_e, n_e, \chi^2) = (9.91, 2.21, 2.75)$. However, for HH 204, the smaller χ^2 values in atom_TZ18_173–coll_TZ18_173 and atom_TZ18_173–SRKFB19_173 indicate improved fits: $\chi^2 = 40.2$. and 64.2 as compared to $\chi^2 = 154$. and 84.7 in the pairs atom_TZ18_52–coll_TZ18_52 and atom_TZ18_52–coll_SRKFB19_52, respectively. Moreover, although the temperatures and densities with coll_SRKFB19_52 and coll_SRKFB19_173 are close, the densities with coll_TZ18_52 and coll_TZ18_173 differ substantially: 2.63 and 1.51, respectively.

4.3.3. Line-Ratio Diagnostics

An extensive discussion of [Fe II] line-ratio diagnostics in the infrared, near-infrared, and optical is given in [29]. Using lines from the HH 202S and HH 204 spectra, we have examined several line ratios to be used as density diagnostics involving "safe" low-energy levels to avoid predicted fluorescence effects [73]. Since temperature diagnostics inherently rely on levels at higher energies, we have refrained from their treatment in the present atomic data comparisons.

We have selected as a showcase in Figure 10 the emissivity ratio $I(\lambda 8892)/I(\lambda 9267)$ that is density sensitive in the range $3 \leq \log n_e \leq 5\,\mathrm{cm}^{-3}$. In the left panel, we plot the emissivity ratio computed with the atom_TZ18_52 radiative dataset and several `coll` ECS files highlighting its dependency on the collisional datasets. We do not show its behavior below $\log n_e = 3$ as it becomes more complicated, manifesting divergences also due to the radiative data. We also include in Figure 10 the observed intensity ratio in HH 202S, $I(\lambda 8892)/I(\lambda 9267) = 2.36 \pm 0.42$, which, except for the curve computed with coll_TZ18_52 ECS, seems to degrade the diagnostic potential of this ratio for $\log n_e \gtrapprox 4.5$ since the density variations lie within its error band. On the other hand, the temperature dependency of the ratio above $T_e \approx 10^4$ K is generally weak, as shown in the right panel.

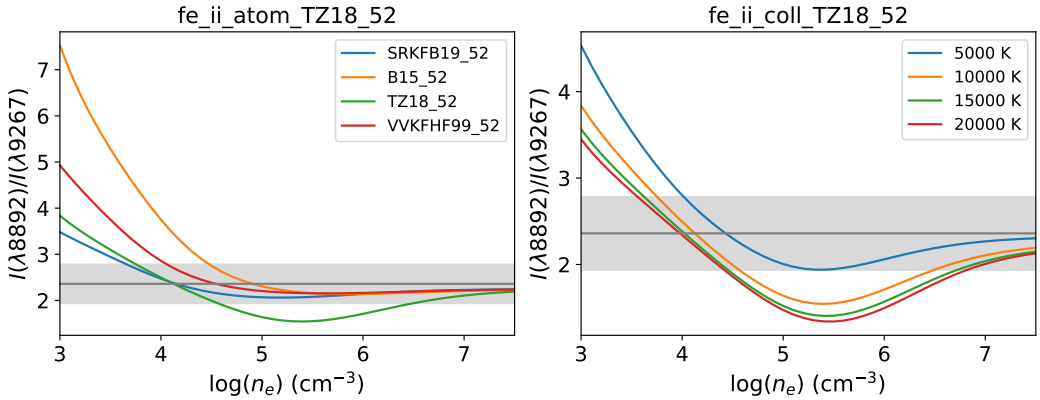

Figure 10. Density behavior of the [Fe II] $I(\lambda 8892)/I(\lambda 9267)$ emissivity ratio using different atomic datasets. The observed ratio in HH 202S is 2.36 ± 0.42, which is depicted as a gray band. **Left panel**: atom_TZ18_52 radiative dataset with four `coll` datasets (SRKFB19_52, B15_52, TZ18_52, VVKFHF99_52) at $T_e = 10^4$ K. **Right panel**: atom_TZ18_52 and coll_TZ18_52 datasets at four electron temperatures.

If this observed line-intensity ratio in HH 202S is used to determine the density, we obtain 7.94×10^4, 1.32×10^4, 1.41×10^4, and 3.55×10^4 cm^{-3} for the `coll` datasets B15_52, TZ18_52, SRKFB19_52, and VVKFHF99_52, respectively, which compare poorly with estimates from the spectrum fits of Section 4.3.2: respectively, 5.98×10^4, 3.29×10^4, 2.21×10^4, and 1.47×10^4 cm^{-3}. Nonetheless, if we take into consideration the gross uncertainties brought about by the collisional datasets, on average, both methods coincide on a similar poor density diagnostic: $(4 \pm 3) \times 10^4$ cm^{-3}.

4.4. Radiative Lifetimes of the $3d^6 4s$, $3d^7$, *and* $3d^5 4s^2$ *Levels*

To compare the lifetimes of levels belonging to the $3d^6 4s$, $3d^7$, and $3d^5 4s^2$ configurations predicted by the `atom` datasets B15_52, DH11_52, TZ18_52, SRKFB19_52, QDZa96, and QDZh96, we again determine an average lifetime for each level by comparing the respective differences for each dataset (see Figure 11). A problematic and identifiable case in this plot is the lowest level of the first excited configuration, $3d^7$ a $^4F_{9/2}$, with the longest lifetime ($\log \overline{\tau} = 4.22$ s) and large discrepant values (~ 0.4 dex). This is an important metastable level inasmuch as being dominant in the plasma radiative and collisional equilibrium and in opening the routes to continuum pumping. In general, the scatter is ~ 0.1 dex, except for lifetimes derived from the A-values of the questionable atom_SRKB19_52 dataset.

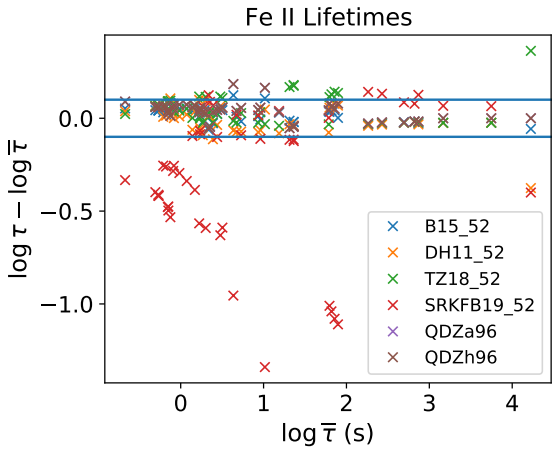

Figure 11. [Fe II] radiative lifetimes for levels within the $3d^6 4s$, $3d^7$, and $3d^5 4s^2$ configurations computed from the A-values in the `atom` datasets B15_52, DH11_52, TZ18_52, SRKFB19_52, QDZa96, and QDZh96. For each level, the lifetime differences for these datasets with respect to the average value are plotted as a function of the average value.

Lifetimes for a handful of metastable levels of [Fe II] have been measured with a laser probing technique, and A-values were derived using branching fractions from the spectra of the Eta Carinae ejecta taken with the *Hubble Space Telescope* [49–51]. A comparison between the experimental lifetimes and those derived from the `PyNeb atom` datasets is given in Table 12. Lifetimes from atom_SRKFB19_52 are markedly discrepant from both the measured and other theoretical values and are thus excluded from this table. The theoretical lifetime of the $3d^6 4s\ b\,^2H_{11/2}$ level shows a large scatter. Although there is good agreement between theory and experiment for the $3d^5 4s^2\ a\,^6S_{5/2}$ level, the rest of the lifetimes from B15_52, DH11_52, and TZ18_52 are generally longer (as long as 33%) than experiment. The best overall agreement with the experiment ($\lesssim 7\%$) is displayed by atom_QDZh96. In Table 13, we compare experimental and theoretical A-values. QDZh96 values are within the experimental error bars except for $A(a\,^4G_{9/2}, a\,^4F_{9/2})$ and $A(b\,^4D_{7/2}, a\,^4F_{7/2})$ for which the theoretical A-values agree to within 12%. The average agreement between the experiment and the rest of the theoretical data is around 20%.

4.5. Radiative Lifetimes of the $3d^6(^5D)4p$ *Odd-Parity Levels*

Radiative lifetimes of the Fe II odd-parity levels $3d^6(^5D)4p$ have been measured with a time-resolved non-linear laser-induced fluorescence technique, whereby an improved signal-to-noise ratio reduces uncertainties to 2–3% [46]. In Table 14, we compare these measurements with lifetimes derived from A-values from atom_TZ18_173 and atom_RKFB19_173. Theoretical lifetimes agree to $\sim 30\%$ but are, on average, around 14% shorter than measurements and well outside the aforementioned error bars.

Experimental E1 A-values were reported using the lifetimes in Table 14 and branching fractions determined with a Fourier transform spectrometer and a high-resolution grating spectrometer to precisions of 6% and 26% for the strong and weak transitions, respectively [46]. We compare these measurements with A-values from atom_TZ18_173 and atom_SRKFB19_173 in Figure 12. A-values from the former dataset with $\log A > 6$ agree with the experiment to within 0.3 dex, while large discrepancies (as large as 3 dex) are displayed by the latter.

4.6. Fe II *gf-Values*

Oscillator strengths (gf-values) for 142 Fe II lines ($\lambda\lambda 4000-8000$) have been derived from both laboratory and computed data and benchmarked with accurate spectra from the Sun and

Table 12. Comparison of [Fe II] experimental lifetimes (in s) with those derived from the revised `PyNeb atom` datasets. The error of the least significant figure of the observed lifetime is indicated in brackets.

	Experiment			Theory				
Level	**Ref. [49]**	**Ref. [50]**	**Ref. [51]**	**B15_52**	**DH11_52**	**TZ18_52**	**QDZa96**	**QDZh96**
$3d^5 4s^2\ a\,^6S_{5/2}$	0.23(3)			0.241	0.233	0.225	0.262	0.220
$3d^6 4s\ a\,^4G_{11/2}$			0.75(10)	0.909	0.960	0.934	0.774	0.706
$3d^6 4s\ a\,^4G_{9/2}$		0.65(2)		0.849	0.862	0.876	0.755	0.694
$3d^6 4s\ b\,^2H_{11/2}$		3.8(3)		5.31	3.71	4.18	6.59	5.20
$3d^6 4s\ b\,^4D_{1/2}$			0.54(3)	0.592	0.627	0.632	0.616	0.550
$3d^6 4s\ b\,^4D_{7/2}$	0.53(3)			0.548	0.578	0.575	0.568	0.501

Table 13. Comparison of experimental A-values (s^{-1}) for transitions in [Fe II] with those listed in the revised `PyNeb atom` datasets. The error of the least significant figure of the observed A-value is indicated in brackets.

			Experiment		Theory				
Upper	**Lower**	**λ_{air} (Å)**	**Ref. [50]**	**Ref. [51]**	**B15_52**	**DH11_52**	**TZ18_52**	**QDZa96**	**QDZh96**
$a\,^4G_{9/2}$	$a\,^4F_{9/2}$	4177.20	0.29(5)		0.16	0.14	0.14	0.18	0.19
	$a\,^4F_{7/2}$	4276.84	0.83(7)		0.66	0.65	0.65	0.75	0.82
	$a\,^4F_{5/2}$	4352.78	0.36(4)		0.31	0.31	0.29	0.35	0.38
$a\,^6S_{5/2}$	$a\,^6D_{9/2}$	4287.39	1.53(22)		1.50	1.55	1.62	1.37	1.65
	$a\,^6D_{7/2}$	4359.33	1.19(21)		1.11	1.15	1.19	1.02	1.22
	$a\,^6D_{5/2}$	4413.78	0.84(13)		0.78	0.81	0.84	0.73	0.86
	$a\,^6D_{3/2}$	4452.10	0.53(8)		0.50	0.52	0.54	0.47	0.55
	$a\,^6D_{1/2}$	4474.90	0.26(4)		0.24	0.25	0.26	0.23	0.27
$b\,^4D_{7/2}$	$a\,^6D_{9/2}$	3175.38	0.23(3)		0.21	0.24	0.21	0.19	0.21
	$a\,^4F_{9/2}$	3376.20	0.96(10)		0.88	0.77	0.81	0.85	0.98
	$a\,^4F_{7/2}$	3440.99	0.23(3)		0.30	0.27	0.28	0.29	0.33
	$a\,^4P_{5/2}$	5551.31	0.18(4)		0.15	0.14	0.14	0.15	0.18
	$a\,^4P_{3/2}$	5613.27	0.10(3)		0.078	0.069	0.075	0.081	0.093
$a\,^4G_{11/2}$	$a\,^4F_{9/2}$	4243.97		1.05(15)	0.85	0.81	0.84	1.02	1.12
	$a\,^4F_{7/2}$	4346.85		0.25(5)	0.20	0.18	0.18	0.23	0.25

metal-poor stars [47]. These gf-values have been compared with data computed with extensive CI using the MCBP code CIV3, including fine-tuning [43]. This calculation included 262 fine-structure levels from the $3d^6 4s$, $3d^7$, $3d^5 4s^2$, $3d^6 4p$, and $3d^5 4s4p$ configurations. In general, good agreement was found except for a few ill-behaved transitions susceptible to effects difficult to constrain computationally such as severe cancellation due to CI mixing.

Table 14. Comparison of experimental lifetimes (in ns) of the $3d^6(^5D)4p$ levels of Fe II with those derived from A-values listed in the revised `PyNeb` `atom` datasets. The error of the least significant figure of the observed lifetime is indicated in brackets.

	Experiment	Theory	
Level	**Ref. [46]**	**TZ18_173**	**SRKFB19_173**
$z\,^6D^o_{9/2}$	3.68(7)	3.17	3.39
$z\,^6D^o_{7/2}$	3.67(9)	3.19	3.43
$z\,^6D^o_{5/2}$	3.69(5)	3.20	3.44
$z\,^6D^o_{3/2}$	3.73(7)	3.21	3.44
$z\,^6D^o_{1/2}$	3.68(11)	3.21	3.45
$z\,^6F^o_{11/2}$	3.20(5)	2.58	2.94
$z\,^6F^o_{9/2}$	3.28(4)	2.63	2.98
$z\,^6F^o_{7/2}$	3.25(6)	2.65	3.09
$z\,^6F^o_{5/2}$	3.30(5)	2.66	3.03
$z\,^6F^o_{3/2}$	3.45(12)	2.67	3.04
$z\,^6P^o_{7/2}$	3.71(4)	2.93	3.53
$z\,^6P^o_{5/2}$	3.75(10)	2.91	3.60
$z\,^6P^o_{3/2}$	3.70(12)	2.89	3.57
$z\,^4D^o_{7/2}$	2.97(4)	2.74	2.10
$z\,^4D^o_{5/2}$	2.90(6)	2.76	2.15
$z\,^4D^o_{3/2}$	2.91(9)	2.74	2.13
$z\,^4F^o_{9/2}$	3.72(10)	3.29	3.14
$z\,^4F^o_{7/2}$	3.59(10)	3.14	3.00
$z\,^4F^o_{5/2}$	3.55(8)	3.16	2.99
$z\,^4P^o_{5/2}$	3.27(6)	3.20	2.74
$z\,^4P^o_{3/2}$	3.23(9)	3.21	2.55

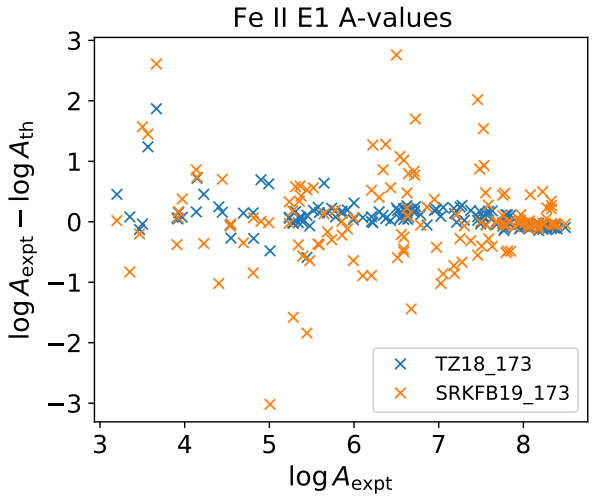

Figure 12. Comparison of experimental A-values (s^{-1}) for E1 transitions arising from the $3d^6(^5D)4p$ levels of Fe II [46] with those from the `atom` datasets TZ18_173 and SRKFB19_173.

In Figure 13, we compare the observed gf-values (MB09) [47] with theoretical data from Ref. [43] (DH14), atom_TZ18_173, and atom_SRKFB19_173. If problematic transitions are excluded, the average agreement of DH14 and atom_TZ18_173 with MB09 is within 0.2 dex.

Dataset atom_SRKFB19_173, on the other hand, contains several transitions with discrepancies greater than 0.5 dex.

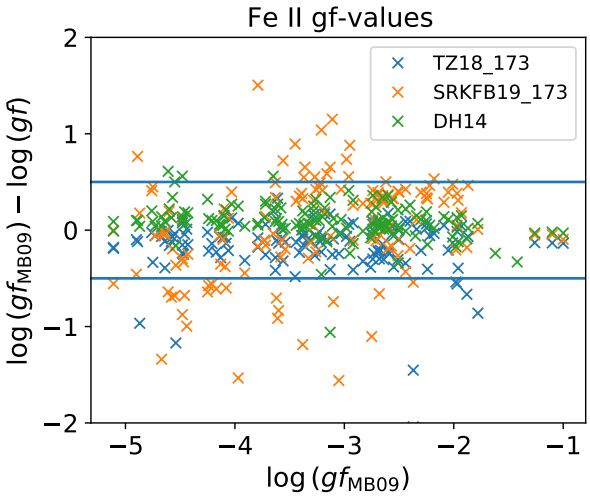

Figure 13. Comparison of observed gf-values for Fe II (MB09) [47] with those calculated from atom_TZ18_173, atom_SRKFB19_173, and Ref. [43] (DH14).

Table 15 shows three transitions for which DH14 shows sizable discrepancies with respect to MB09. Datasets atom_TZ18_173 and atom_SRKFB19_173 do not perform much better; thus, the hindrance from cancellation effects in computational estimates put forward in Ref. [43] is reinforced. This table also lists three transitions we were not able to identify in atom_TZ18_173 or atom_SRKFB19_173 for which the agreement between DH14 and MB09 is reasonable.

Table 15. Problematic transitions in the gf-value comparison of MB09 [47] with atom_TZ18_173, atom_SRKFB19_173, and DH14 [43] showing large discrepancies or unidentified lines.

			MB09	**TZ18_173**	**SRKFB19_173**	**DH14**
Lower	Upper	λ_{air} (Å)		$\log(gf)$		
$3d^64p\ z\ ^4F^o_{5/2}$	$3d^54s^2\ c\ ^4D_{3/2}$	6508.13	−3.45	−3.93	−2.56	−7.90
$3d^64s\ c\ ^4F_{9/2}$	$3d^64p\ x\ ^4G^o_{9/2}$	6433.81	−2.37	−3.82	−2.91	−4.41
$3d^64p\ z\ ^4F^o_{7/2}$	$3d^54s^2\ c\ ^4D_{5/2}$	6371.13	−3.13	−3.54	−2.48	−4.19
		4635.32	−1.42			−1.75
		4625.89	−2.35			−2.41
		4549.19	−1.62			−1.86

4.7. Fe II Branching Fractions

Branching fractions

$$BF_{ji} = \frac{I(j,i)}{\sum_i I(j,i)} = \frac{A(j,i)}{\sum_i A(j,i)} \quad (4)$$

for 121 Fe II UV lines originating from levels of the $3d^6(^5D)4p$ configuration have been measured in low-current spectra from Fe–Ne and Fe–Ar hollow cathode discharge lamps. The spectra were taken with a UW 3 m echelle spectrograph with a resolving power of 250,000 [48]. We compare these branching fractions in Figure 14 with those derived from A-values of the atom_TZ18_173 and atom_SRKFB19_173 `atom` datasets. For transitions with $\log(BF_{expt}) > -2$, the branching fractions from atom_TZ18_173 agree with the experiment, on average, to better

than 30%, while significantly larger discrepancies are displayed by atom_SRKFB19_173. However, most theoretical branching fractions, in general, do not match the accuracy implicit in the experimental error bars.

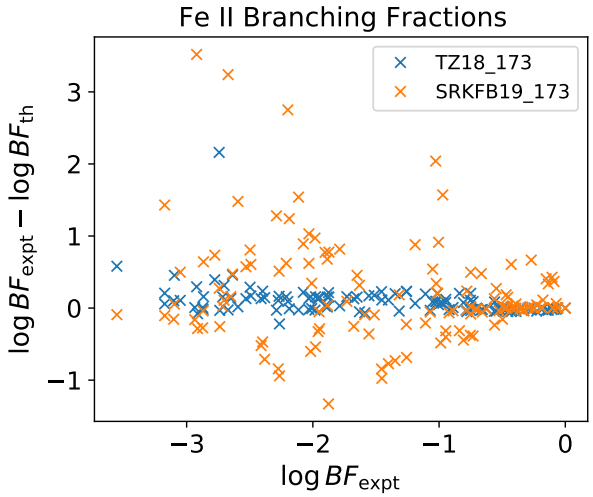

Figure 14. Comparison of Fe II experimental branching fractions (BF_{expt}) [48] with theoretical values (BF_{th}) derived from atom_TZ18_173 and atom_SRKFB19_173.

4.8. [Fe II] Effective Collision Strengths

We have constructed three revised `coll` datasets containing ECS for the [Fe II] 52-level atomic model of `PyNeb`: B15_52, TZ18_52, and SRKFB19_52. We determine for each transition the average ECS from these three datasets at $T = 10^4$ K, and as depicted in Figure 15, we compare the logarithmic differences with respect to this average. ECS from coll_B15_52 appear to lie below average, displaying differences as large as $\Delta \log \Upsilon \approx -4$, while those from coll_SRKFB19_52 are above average with a scatter within 1.0 dex. The most interesting result is coll_TZ18_52 with an ECS average well within 0.5 dex. This outcome supports the findings in the spectrum fits (see Table 11), whereby the electron densities predicted by coll_B15_52 are higher, coll_SRKFB19_52 lower, and coll_TZ18_52 in between.

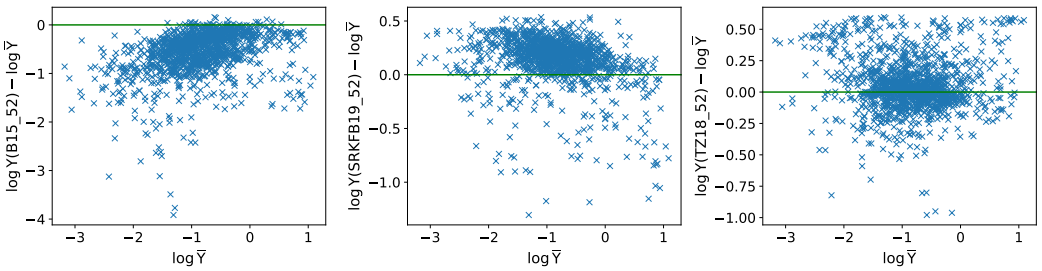

Figure 15. [Fe II] ECS logarithmic differences at $T = 10^4$ K for each transition in the `coll` datasets B15_52, SRKFB19_52, and TZ18_52 relative to the average value.

Due to the diagnostic potential of [Fe II] emission lines in interstellar-medium plasmas, accurate ECS at low temperatures were recently computed for transitions among levels of the $3d^6(^5D)4s\,a\,^6D_J$ ground term [36]. To obtain uncertainty estimates, different target models and relativistic R-matrix methods (BPRM, ICFT, DARC) were used in these calculations. In Figure 16, we compare selected ECS from [36] with those from `coll` datasets B15_52, TZ18_52, and SRKFB19_52. For this purpose, we use the `PyNeb` `getOmega(T,j,i)` function that allows

ECS linear interpolation at the input temperature `T`; if the latter lies outside the temperature range of the tabulated ECS, the function lists the end value. This is the case of coll_B15_52 and coll_SRKFB19_52 for $\log T < 3$ (see Figure 16). As expected, the best agreement is with coll_SRKFB19_52, although there are points outside the error bars. Large discrepancies are also found with coll_B15_52 and coll_TZ18_52 at higher temperatures ($\log T > 4$).

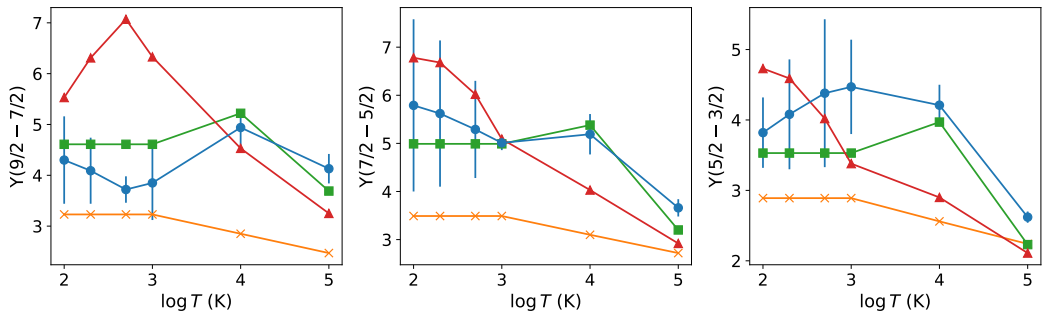

Figure 16. ECS $\Upsilon(J - J')$ for the transitions $3d^6(^5D)4s\ a\ ^6D_J - a\ ^6D_{J'}$ within the ground term of [Fe II]. Blue circles: Ref. [36]. Yellow crosses: coll_B15_52. Green squares: coll_SRKFB19_52. Red triangles: coll_TZ18_52.

4.9. Fe II Discussion

In the implementation of new datasets for [Fe II], we found term misassignments for levels with total orbital angular momentum quantum number $L = 5$ in the atomic model of atom_SRKFB19_225 (see Table 6). A further comparison in Table 7 of A-values for transitions arising from the $3d^64s\ a\ ^4H_J$ and $3d^64s\ b\ ^2H_J$ ($J = 9/2$ and $11/2$) levels indicate large discrepancies with respect to other `atom` datasets (TZ18_225, DH11_52, B15_52, QDZa96, and QDZh96). This is an indication of faulty data that can be corroborated with the discrepancies displayed by dataset atom_SRKFB19_52 in the comparison of observed and computed A-value ratios carried out in Section 4.3.1.

This comparison also brings out observed lines with questionable identifications (e.g., $\lambda\lambda 3968.27, 4889.71$) and unreliable line-intensity ratios—e.g., $I(\lambda 7637.52)/I(\lambda 9051.95)$, $I(\lambda 7686.93)/I(\lambda 8891.93)$, and $I(\lambda 7733.13)/I(\lambda 9033.49)$—due to A-values with magnitude $\log A \lesssim -3$. Theoretical A-value ratios agree to within 20–25% and, with respect to the observed line-intensity ratios, to within the error bars except for some outliers subject to strong level mixing, as pointed out in [40].

We have found atomic data files, namely atom_B15 and coll_B15, with faulty data caused again by the incorrect mapping to atomic models with different level numbering. This problem is exacerbated by data producers who use several multi-configuration methods implementing a variety of relativistic Hamiltonians (Dirac–Fock, Breit–Pauili, Pauli). This multi-code approach may enable accuracy estimates of the radiative and collisional data, but it often leads to level structures with conflicting numbering and identifications that are difficult to remap. The use of fine-tuning in atomic calculations to match the experimental level order does mitigate this problem.

In contrast to [Fe III], for which the spectrum fits using different atomic datasets resulted in acceptable temperature (6%) and density (20%) uncertainties thus sustaining their reliability, for [Fe II], the collisional datasets lead to temperature variations of around 15–20% and density discrepancies as large as a factor of four. However, the reasonable temperature and density accord between coll_SRKFB19_52 and coll_VVKFHF99_52 must be noted. These results appear to indicate that, for [Fe II], the electron density is not a good fitting parameter or, as previously proposed [72–74], fluorescence continuum pumping might be a level-populating mechanism we have not taken into account. Furthermore, the extremely low critical density of level $3d^7\ a\ ^4F_{9/2}$

(see Figure 8) and its sensitivity to both the radiative and collisional datasets (Figure 9) give this level a protagonistic role in the [Fe II] spectrum formation, notwithstanding the poor accuracy of its small A-value.

The potential of line-ratio density diagnostics in [Fe II] is compromised by the mismatch with the spectrum fits, and the temperature diagnostics are discouraged by the looming role of fluorescence pumping. In Section 4.3.3, we use the $I(\lambda 8892)/I(\lambda 9267)$ ratio to illustrate a density diagnostic problem: the density variations in the range of interest ($3 \leq \log n_e \leq 5\,\mathrm{cm}^{-3}$) lie within the observed line-intensity error band. As performed in Section 3.3.3 for the analysis of the [Fe III] density diagnostics, an observational sample of low-density ionized nebulae with [Fe II] detections would be helpful to constrain the predictions of both the radiative and collisional parameters. The lack of such a sample in the literature prevents us from drawing further conclusions.

We have performed extensive comparisons of computed and measured radiative data for both the $3d^64s$, $3d^7$, and $3d^54s^2$ even-parity levels and the $3d^64p$ and $3d^54s4p$ odd-parity levels. Regarding even-parity levels (see Section 4.4), the computed radiative lifetimes agree to within 0.1 dex except for the singular $3d^7$ a $^4F_{9/2}$ metastable level with $\log\tau \sim 4\,\mathrm{s}$ and an uncertainty of 0.4 dex. It must be noted that the A-values in atom_SRKB19_52 display questionable lifetimes for some of these levels (see Figure 11). The best overall agreement between theory and experiment ($\sim 7\%$) is with the atom_QDZh96 dataset, while other `atom` datasets (B15_52, DH11_52, and TZ18_52) in general yield longer (as long as 33%) lifetimes than experiment. As discussed in [40], the large uncertainty of the $3d^64s$ b $^2H_{11/2}$ lifetime is caused by imprecise level mixing. A-values derived from the experimental lifetimes, on average, agree to around 20% with those in the theoretical datasets.

Accurate (2–3%) radiative lifetimes have been measured for the $3d^6(^5D)4p$ odd-parity levels [46], which have been compared in Section 4.5 with those derived from the atom_TZ18_173 and atom_SRKFB19_173 datasets. Theoretical lifetimes agree to within 30%, but on average they are around 14% shorter than measurements. E1 A-values have also been derived from these lifetime measurements, and those with $\log A > 6$ agree with atom_TZ18_173 to within 0.3 dex while larger discrepancies (as large as 3 dex) are found in atom_SRKFB19_173. Moreover, the comparison of the observed gf-values [47] in Section 4.6 with those derived from the theoretical datasets shows good agreement (0.2 dex) with atom_TZ18_173 and discrepancies larger than 0.5 dex with atom_SRKFB19_173. A similar outcome is obtained in the comparison of measured branching ratios [48] in Section 4.7, whereby those derived from A-values in atom_TZ18_173 with $\log(BF_{\mathrm{expt}}) > -2$ agree to better than 30%, while some from atom_SRKFB19_173 show larger discrepancies. In general, the theoretical radiative datasets do not reach anywhere near the accuracy quoted for the measured lifetimes, A-values, gf-values, and branching fractions.

The comparison of collisional datasets in Figure 15 of Section 4.8 gives a macro-measure of the overall ECS magnitudes that has a direct impact on the critical densities. In this comparison, we determined for each transition an average ECS using three `coll` datasets (B15_52, SRKFB19_52, and TZ18_52) and then plotted the dispersion for each dataset. Figure 15 shows that the smallest dispersion (within 0.5 dex) is by coll_TZ18_52 while differences in coll_B15_52 and coll_SRKFB19_52 are larger and, respectively, mostly negative and positive. The fairly large ECS discrepancies found in Figure 16 for transitions within the $3d^6(^5D)4s$ a ^6D ground term at low temperatures gives a further indication of the patchy quality of the collisional data for Fe II.

From the extensive data tests hereby carried out on the Fe II datasets, we find the radiative data in atom_SRKFB19_52 to be faulty, and this could indeed have an impact on the coll_SRKFB19_52 data. We would therefore select as the `PyNeb` 1.1.17 defaults the atom_TZ18_173 and coll_ TZ18_173 datasets.

5. Conclusions

We have performed extensive data evaluations of the `levels`, `atom`, and `coll` files for [Fe III] and [Fe II] in `PyNeb` 1.1.16 to examine their worthiness in nebular spectral modeling and to select the package defaults. In most cases, we have reconstructed the datasets from the sources and introduced newly published data, thus leading to a more reliable atomic database for these species in the new release `PyNeb` 1.1.17.

The present data assessment comprises: fits of high-resolution spectra from the HH 202S and HH 204 Herbig–Haro objects taken with the Ultraviolet Visual Echelle Spectrograph [9, 11]; comparisons of theoretical and observed line-intensity ratios; and comparisons with measurements of radiative lifetimes, A-values, gf-values, and branching ratios. Observed lines may suffer from misidentifications, line blending, and telluric or instrumental contamination. On the other hand, the computation of accurate radiative data for lowly ionized ions of the iron group with open $3d^n$ shells is hindered by strong configuration mixing, double-excitation representations, and subtle core–valence correlation involving closed and open subshells; thus, broadly speaking, we would not expect an A-value accuracy of better than 20%. Similarly, the ECS at low temperatures are affected by complex resonance structures sensitive to target models and channel convergence that seriously compromise accuracy ratings.

For Fe III, we introduced a new `levels` file from the NIST database with more complete level assignments and accurate energies. The previous version of the `levels` file is in the `deprecated` directory, renamed as `fe_iii_levels_2023.dat`. As described in Section 3.2, we implemented the new `atom` files Q96_34, DH09_34, BBQ10_34, BB14_34, and BB14_144 and the `coll` files Z96_34, BBQ10_34, BB14_34, Z96_144, and BB14_144. In `PyNeb` 1.1.17 atom_BBQ10_34, atom_BB14_34, coll_Z96_34 are not included as they are, respectively, made redundant by atom_BBQ10, atom_BB14_144, and coll_Z96_144 while coll_BB14 and coll_BBQ10 are deprecated.

A comparison of the observed line-intensity ratios for transitions arising from the same upper level in [Fe III] with the corresponding A-value ratios constrains the overall accuracy of the latter to around 20–30%. Spectrum fits with the new datasets led to temperatures and densities within 6% and 20%, respectively, validating their usefulness. Radiative lifetimes computed with these `atom` datasets agree to within 0.1 dex. A revision of `coll` files brings out the incompleteness of the Z96_34 dataset and its poor accuracy for ECS with $\log \Upsilon < -1$. For [Fe III], we have selected the atom_BB14_144 and coll_BB14_144 datasets as the defaults in `PyNeb` 1.1.17.

For Fe II, we have implemented the `atom` files VVKFHF99_52, DH11_52, B15_52, TZ18_52, SRKFB19_52, TZ18_173, SRKFB19_173 and `coll` files VVKFHF99_52, B15_52, TZ18_52, SRKFB19_52, TZ18_173, and SRKFB19_173. After extensive tests and much pondering, the atom_SRKFB19_52 and atom_SRKFB19_173 datasets were found to contain faulty A-values, while atom_VVKFHF99_52 and coll_VVKFHF99_52 have missing data; therefore, these files are not included in `PyNeb` 1.1.17. Apart from this drawback, the theoretical A-value ratios for transitions arising from a common upper level derived from the rest of the `atom` files agree to within 20–25%, and most lie within the experimental error bars. The spectrum fits yielded temperature and density variations of around 20% and a factor of 4, respectively, which appear to indicate that the density is not a good fitting parameter and fluorescence continuum pumping might be a level-populating contributor not taken into account. However, the poor theoretical characterization of the key level $3d^7\ a\ ^4F_{9/2}$, inasmuch as its inaccurate A-value and extremely low critical density sensitive to both the radiative and collisional datasets, deters us from more conclusive remarks. Extensive comparisons of the radiative data for both forbidden and allowed transitions with experiment bring out the computational difficulties to match the measured accuracy (better than 10%); thus, a global theoretical A-value accuracy of 20–30% would be statistically

sound. Finally, the examined `coll` datasets lead to different critical densities around $T_e = 10^4$ K, a situation that is difficult to analyze.

In `PyNeb` 1.1.17, the `atom` files VVKFHF99_52, TZ18_52 and `coll` files VVKFHF99_52, SRKFB19_52, SRKFB19_173 are made redundant by atom_VVKFHF99, atom_TZ18_173, coll_VVKFHF99, and coll_SRKFB19. Furthermore, atom_B15, coll_B15, atom_VVKFHF99, coll_VVKFHF99 are deprecated. We select atom_TZ18_173 and coll_TZ18_173 as defaults.

The status of all the data files for Fe III and Fe II in `PyNeb` 1.1.16 and 1.1.17 are summarized in Table A1 of Appendix A.

A final recommendation emerging from the present work must be put forward regarding the curation of the atomic databases associated with spectral modeling codes. The potential of the latter in astrophysical analyses relies in great part on the integrity (accuracy and completeness) of their tabulations of radiative and collisional rates, which, as shown here, demand detailed evaluation and upgrading. For complex ionic spectra such as [Fe III] and [Fe II], this may imply a lengthy endeavor.

Author Contributions: C.M. (Claudio Mendoza) conceptualized and coordinated the full paper. J.E.M.-D. and J.G.-R. provided the observational data and extensive discussions about their validity and provenance. M.A.B. provided data, performed calculations, and led discussions about fluorescence continuum pumping in [Fe II]. C.M. (Christophe Morisset) researched data, performed ancillary calculations, and software support regarding the `PyNeb` package. Investigation, methodology, analysis, and validation: C.M. (Claudio Mendoza), J.E.M.-D., J.G.-R., M.A.B., C.M. (Christophe Morisset). Writing and original draft preparation: C.M. (Claudio Mendoza), J.E.M.-D. Review and editing: C.M. (Claudio Mendoza), J.E.M.-D., C.M. (Christophe Morisset), J.G.-R., M.A.B. Visualization: C.M. (Claudio Mendoza), J.E.M.-D. All authors have read and agreed to the published version of the manuscript.

Funding: J.E.M.-D. acknowledges funding from the Deutsche Forschungsgemeinschaft (DFG, German Research Foundation) in the form of an Emmy Noether Research Group (grant number KR4598/2-1, PI Kathryn Kreckel). Ch.M. acknowledges the support from UNAM/DGAPA/PAPIIT grant IN101220. J.G.-R. acknowledges support from an Advanced Fellowship under the Severo Ochoa excellence program CEX2019-000920-S; financial support from the Canarian Agency for Research, Innovation, and Information Society (ACIISI) of the Canary Islands Government and the European Regional Development Fund (ERDF) under grant with reference ProID2021010074; and support under grant P/308614 financed by funds transferred from the Spanish Ministry of Science, Innovation, and Universities (MCIU) charged to the General State Budgets and with funds transferred from the General Budgets of the Autonomous Community of the Canary Islands by the MCIU.

Data Availability Statement: The data files revised and compiled for this revision are publicly available in `PyNeb` 1.1.17.

Acknowledgments: We acknowledge extensive private communications and data exchange with Catherine Ramsbottom (Queen's University Belfast, UK) regarding the radiative and collisional data for Fe II. We are indebted to Grażyna Stasińska (Observatoire de Paris, France) for data exchange and useful discussions.

Conflicts of Interest: The authors declare no conflict of interest.

Abbreviations

The following abbreviations are used in this manuscript:

CDS	Centre de Données astronomiques de Strasbourg
NIST	National Institute os Standards and Technology

Appendix A

Table A1. Status of the Fe III and Fe II atomic data files in the `PyNeb` library for versions 1.1.16 and 1.1.17. 'X' means the file is present; '*' means the file is present and is the default; 'D' means the file is deprecated (but may still be accessible with the command `pn.atomicData.includeDeprecatedPath()`).

Fe III File Name	v1.1.16	v1.1.17	Fe II File Name	v1.1.16	v1.1.17
fe_iii_atom_BB14_144.dat		*	fe_ii_atom_TZ18_173.dat		*
fe_iii_atom_BBQ10.dat	X	X	fe_ii_atom_B15.dat	*	D
fe_iii_atom_DH09_34.dat		X	fe_ii_atom_B15_52.dat		X
fe_iii_atom_NP96.dat	X	X	fe_ii_atom_DH11_52.dat		X
fe_iii_atom_Q96_34.dat		X	fe_ii_atom_SRKFB19.dat	X	D
fe_iii_atom_Q96_J00.dat	*	X	fe_ii_atom_VVKFHF99.dat	X	D
fe_iii_coll_BB14_144.dat		*	fe_ii_coll_TZ18_173.dat		*
fe_iii_coll_BB14.dat	X	D	fe_ii_coll_B15.dat	*	D
fe_iii_coll_BBQ10.dat	X	D	fe_ii_coll_B15_52.dat		X
fe_iii_coll_BBQ10_34.dat		X	fe_ii_coll_B15_old.dat	X	D
fe_iii_coll_Q96.dat	X	X	fe_ii_coll_SRKFB19.dat	X	X
fe_iii_coll_Z96.dat	*	X	fe_ii_coll_VVKFHF99.dat	X	D
fe_iii_coll_Z96_144.dat		X			

Notes

[1] http://research.iac.es/proyecto/PyNeb/

[2] http://cdsweb.u-strasbg.fr/topbase/testop/TheIP.html

[3] https://open.adas.ac.uk/

References

1. Luridiana, V.; Morisset, C.; Shaw, R.A. PyNeb: A New Software for the Analysis of Emission Lines. In *IAU Symposium*; Cambridge University Press: Cambridge, UK, 2012; Volume 283, pp. 422–423. https://doi.org/10.1017/S1743921312011738.
2. Luridiana, V.; Morisset, C.; Shaw, R.A. PyNeb: A new tool for analyzing emission lines. I. Code description and validation of results. *Astron. Astrophys.* **2015**, *573*, A42. https://doi.org/10.1051/0004-6361/201323152.
3. Peimbert, M.; Peimbert, A.; Delgado-Inglada, G. Nebular Spectroscopy: A Guide on H II Regions and Planetary Nebulae. *Publ. Astron. Soc. Pac.* **2017**, *129*, 082001. https://doi.org/10.1088/1538-3873/aa72c3.
4. Morisset, C.; Luridiana, V.; García-Rojas, J.; Gómez-Llanos, V.; Bautista, M.; Mendoza., Claudio. Atomic Data Assessment with PyNeb. *Atoms* **2020**, *8*, 66. https://doi.org/10.3390/atoms8040066.
5. Juan de Dios, L.; Rodríguez, M. Atomic data and the density structures of planetary nebulae. *Mon. Not. R. Astron. Soc.* **2021**, *507*, 5331–5339. https://doi.org/10.1093/mnras/stab2488.
6. Perinotto, M.; Bencini, C.G.; Pasquali, A.; Manchado, A.; Rodriguez Espinosa, J.M.; Stanga, R. The iron abundance in four planetary nebulae. *Astron. Astrophys.* **1999**, *347*, 967–974.
7. Delgado Inglada, G.; Rodríguez, M.; Mampaso, A.; Viironen, K. The Iron Abundance in Galactic Planetary Nebulae. *Astrophys. J.* **2009**, *694*, 1335–1348, https://doi.org/10.1088/0004-637X/694/2/1335.
8. Delgado-Inglada, G.; Mesa-Delgado, A.; García-Rojas, J.; Rodríguez, M.; Esteban, C. The Fe/Ni ratio in ionized nebulae: Clues on dust depletion patterns. *Mon. Not. R. Astron. Soc.* **2016**, *456*, 3855–3865, https://doi.org/10.1093/mnras/stv2961.
9. Mesa-Delgado, A.; Esteban, C.; García-Rojas, J.; Luridiana, V.; Bautista, M.; Rodríguez, M.; López-Martín, L.; Peimbert, M. Properties of the ionized gas in HH 202—II. Results from echelle spectrophotometry with Ultraviolet Visual Echelle Spectrograph. *Mon. Not. R. Astron. Soc.* **2009**, *395*, 855–876, https://doi.org/10.1111/j.1365-2966.2009.14554.x.
10. Méndez-Delgado, J.E.; Esteban, C.; García-Rojas, J.; Henney, W.J.; Mesa-Delgado, A.; Arellano-Córdova, K.Z. Photoionized Herbig-Haro objects in the Orion Nebula through deep high-spectral resolution spectroscopy—I. HH 529 II and III. *Mon. Not. R. Astron. Soc.* **2021**, *502*, 1703–1739, https://doi.org/10.1093/mnras/stab068.
11. Méndez-Delgado, J.E.; Henney, W.J.; Esteban, C.; García-Rojas, J.; Mesa-Delgado, A.; Arellano-Córdova, K.Z. Photoionized Herbig-Haro Objects in the Orion Nebula through Deep High Spectral Resolution Spectroscopy. II. HH 204. *Astrophys J.* **2021**, *918*, 27. https://doi.org/10.3847/1538-4357/ac0cf5.

12. D'Odorico, S.; Cristiani, S.; Dekker, H.; Hill, V.; Kaufer, A.; Kim, T.; Primas, F. Performance of UVES, the echelle spectrograph for the ESO VLT and highlights of the first observations of stars and quasars. In Discoveries and Research Prospects from 8- to 10-Meter-Class Telescopes; Bergeron, J., Ed.; Society of Photo-Optical Instrumentation Engineers (SPIE): Bellingham, WA, USA, 2000; Volume 4005, pp. 121–130. https://doi.org/10.1117/12.390133.
13. Garstang, R.H. Transition probabilities for forbidden lines of Fe II. *Mon. Not. R. Astron. Soc.* **1962**, *124*, 321. https://doi.org/10.1093/mnras/124.4.321.
14. Kurucz, R.L.; Peytremann, E. *A Table of Semiempirical gf Values. Pt 1: Wavelengths: 5.2682 NM to 272.3380 nm; Pt 2: Wavelengths: 272.3395 NM to 599.3892 nm; Pt 3: Wavelengths: 599.4004 NM to 9997.2746 NM*; SAO Special Report; Smithsonian Astrophysical Observatory: Cambridge, MA, USA, 1975.
15. Nussbaumer, H.; Storey, P.J. Atomic data for Fe II. *Astron. Astrophys.* **1980**, *89*, 308–313.
16. Nussbaumer, H.; Pettini, M.; Storey, P.J. Sextet transitions in Fe II. *Astron. Astrophys.* **1981**, *102*, 351–358.
17. Hummer, D.G.; Berrington, K.A.; Eissner, W.; Pradhan, A.K.; Saraph, H.E.; Tully, J.A. Atomic data from the IRON project. I. Goals and methods. *Astron. Astrophys* **1993**, *279*, 298–309.
18. Eissner, W.; Jones, M.; Nussbaumer, H. Techniques for the calculation of atomic structures and radiative data including relativistic corrections. *Comput. Phys. Commun.* **1974**, *8*, 270–306. https://doi.org/10.1016/0010-4655(74)90019-8.
19. Hibbert, A. CIV3—A general program to calculate configuration interaction wave functions and electric-dipole oscillator strengths. *Comput. Phys. Commun.* **1975**, *9*, 141–172. https://doi.org/10.1016/0010-4655(75)90103-4.
20. Cowan, R.D. *The Theory of Atomic Structure and Spectra*; University of California: Berkeley, CA, USA, 1981.
21. Nahar, S.N. Atomic data from the Iron Project. VII. Radiative dipole transition probabilities for Fe II. *Astron. Astrophys.* **1995**, *293*, 967–977.
22. Nahar, S.N.; Pradhan, A.K. Atomic data from the Iron Project. XVII. Radiative transition probabilities for dipole allowed and forbidden transitions in Fe III. *Astron. Astrophys. Suppl. Ser.* **1996**, *119*, 509–522.
23. Quinet, P.; Le Dourneuf, M.; Zeippen, C.J. Atomic data from the IRON Project. XIX. Radiative transition probabilities for forbidden lines in Fe II. *Astron. Astrophys. Suppl. Ser.* **1996**, *120*, 361–371.
24. Zhang, H.L.; Pradhan, A.K. Atomic data from the Iron Project. VI. Collision strengths and rate coefficients for Fe II. *Astron. Astrophys.* **1995**, *293*, 953–966.
25. Zhang, H. Atomic data from the Iron Project. XVIII. Electron impact excitation collision strengths and rate coefficients for Fe III. *Astron. Astrophys. Suppl. Ser.* **1996**, *119*, 523–528.
26. Bautista, M.A.; Pradhan, A.K. Atomic data from the Iron project. XIII. Electron excitation rates and emissivity ratios for forbidden transitions in Ni II and Fe II. *Astron. Astrophys. Suppl. Ser.* **1996**, *115*, 551–559.
27. Bautista, M.A.; Ballance, C.P.; Quinet, P. Atomic Data and Spectral Model for Fe III. *Astrophys. J.* **2010**, *718*, L189–L193. https://doi.org/10.1088/2041-8205/718/2/L189.
28. Badnell, N.R.; Ballance, C.P. Electron-impact Excitation of Fe^{2+}: A Comparison of Intermediate Coupling Frame Transformation, Breit-Pauli and Dirac R-matrix Calculations. *Astrophys. J.* **2014**, *785*, 99. https://doi.org/10.1088/0004-637X/785/2/99.
29. Bautista, M.A.; Fivet, V.; Ballance, C.; Quinet, P.; Ferland, G.; Mendoza, C.; Kallman, T.R. Atomic Data and Spectral Model for Fe II. *Astrophys. J.* **2015**, *808*, 174. https://doi.org/10.1088/0004-637X/808/2/174.
30. Tayal, S.S.; Zatsarinny, O. Electron-impact excitation of forbidden and allowed transitions in Fe II. *Phys. Rev. A* **2018**, *98*, 012706. https://doi.org/10.1103/PhysRevA.98.012706.
31. Smyth, R.T.; Ramsbottom, C.A.; Keenan, F.P.; Ferland, G.J.; Ballance, C.P. Towards converged electron-impact excitation calculations of low-lying transitions in Fe II. *Mon. Not. R. Astron. Soc.* **2019**, *483*, 654–663. https://doi.org/10.1093/mnras/sty3198.
32. Berrington, K.A.; Eissner, W.B.; Norrington, P.H. RMATRX1: Belfast atomic R-matrix codes. *Comput. Phys. Commun.* **1995**, *92*, 290–420. https://doi.org/10.1016/0010-4655(95)00123-8.
33. Zatsarinny, O. BSR: B-spline atomic R-matrix codes. *Comput. Phys. Commun.* **2006**, *174*, 273–356. https://doi.org/10.1016/j.cpc.2005.10.006.
34. Ait-Tahar, S.; Grant, I.P.; Norrington, P.H. Electron scattering by Fe XXII within the Dirac R-matrix approach. *Phys. Rev. A* **1996**, *54*, 3984–3989. https://doi.org/10.1103/PhysRevA.54.3984.
35. Griffin, D.C.; Badnell, N.R.; Pindzola, M.S. **R**-matrix electron-impact excitation cross sections in intermediate coupling: An MQDT transformation approach. *J. Phys. B At. Mol. Phys.* **1998**, *31*, 3713–3727. https://doi.org/10.1088/0953-4075/31/16/022.
36. Wan, Y.; Favreau, C.; Loch, S.D.; McLaughlin, B.M.; Qi, Y.; Stancil, P.C. Electron-impact fine-structure excitation of Fe II at low temperature. *Mon. Not. R. Astron. Soc.* **2019**, *485*, 2252–2258. https://doi.org/10.1093/mnras/stz550.
37. Deb, N.C.; Hibbert, A. Oscillator strengths for transitions among Fe III levels belonging to the three lowest configurations. *J. Phys. Conf. Ser.* ***2008***, 130, *012006*. https://doi.org/10.1088/1742-6596/130/1/012006.
38. Deb, N.C.; Hibbert, A. Electric quadrupole and magnetic dipole transitions among $3d^6$ levels of Fe III. *J. Phys. B Atom. Mol. Phys.* **2009**, *42*, 065003. https://doi.org/10.1088/0953-4075/42/6/065003.

39. Deb, N.C.; Hibbert, A. Weighted f-values, A-values, and line strengths for the E1 transitions among 3d ^{6}, 3d ^{5}4s, and 3d ^{5}4p levels of Fe III. *Atom. Data Nucl. Data Tables.* **2009**, *95*, 184–303. https://doi.org/10.1016/j.adt.2008.12.001.
40. Deb, N.C.; Hibbert, A. Importance of level mixing on accurate [Fe II] transition rates. *Astron. Astrophys.* **2010**, *524*, A54. https://doi.org/10.1051/0004-6361/201015426.
41. Deb, N.C.; Hibbert, A. Calculation of Intensity Ratios of Observed Infrared [Fe II] Lines. *Astrophys. J.* **2010**, *711*, L104–L107. https://doi.org/10.1088/2041-8205/711/2/L104.
42. Deb, N.C.; Hibbert, A. Radiative transition rates for the forbidden lines in Fe II. *Astron. Astrophys.* **2011**, *536*, A74. https://doi.org/10.1051/0004-6361/201118059.
43. Deb, N.C.; Hibbert, A. log gf values for astrophysically important transitions Fe II. *Astron. Astrophys.* **2014**, *561*, A32. https://doi.org/10.1051/0004-6361/201322751.
44. Quinet, P. Transition probabilities for forbidden lines of Fe III. *Astron. Astrophys. Suppl. Ser.* **1996**, *116*, 573–578.
45. Fivet, V.; Quinet, P.; Bautista, M.A. Radiative rates for forbidden M1 and E2 transitions of astrophysical interest in doubly ionized iron-peak elements. *Astron. Astrophys* **2016**, *585*, A121. https://doi.org/10.1051/0004-6361/201526983.
46. Schnabel, R.; Schultz-Johanning, M.; Kock, M. Fe II lifetimes and transition probabilities. *Astron. Astrophys.* **2004**, *414*, 1169–1176. https://doi.org/10.1051/0004-6361:20031685.
47. Meléndez, J.; Barbuy, B. Both accurate and precise gf-values for Fe II lines. *Astron. Astrophys.* **2009**, *497*, 611–617. https://doi.org/10.1051/0004-6361/200811508.
48. Den Hartog, E.A.; Lawler, J.E.; Sneden, C.; Cowan, J.J.; Brukhovesky, A. Atomic Transition Probabilities for UV and Blue Lines of Fe II and Abundance Determinations in the Photospheres of the Sun and Metal-poor Star HD 84937. *Astrophys. J. Suppl, Ser.* **2019**, *243*, 33. https://doi.org/10.3847/1538-4365/ab322e.
49. Rostohar, D.; Derkatch, A.; Hartman, H.; Johansson, S.; Lundberg, H.; Mannervik, S.; Norlin, L.O.; Royen, P.; Schmitt, A. Lifetime Measurements of Metastable States in Fe^+. *Phys. Rev. Lett.* **2001**, *86*, 1466–1469. https://doi.org/10.1103/PhysRevLett.86.1466.
50. Hartman, H.; Derkatch, A.; Donnelly, M.P.; Gull, T.; Hibbert, A.; Johansson, S.; Lundberg, H.; Mannervik, S.; Norlin, L.O.; Rostohar, D.; et al. The FERRUM Project: Experimental transition probabilities of [Fe II] and astrophysical applications. *Astron. Astrophys.* **2003**, *397*, 1143–1149. https://doi.org/10.1051/0004-6361:20021557.
51. Gurell, J.; Hartman, H.; Blackwell-Whitehead, R.; Nilsson, H.; Bäckström, E.; Norlin, L.O.; Royen, P.; Mannervik, S. The FERRUM project: Transition probabilities for forbidden lines in [Fe II] and experimental metastable lifetimes. *Astron. Astrophys.* **2009**, *508*, 525–529. https://doi.org/10.1051/0004-6361/200913233.
52. Johansson, S.; Zethson, T.; Hartman, H.; Ekberg, J.O.; Ishibashi, K.; Davidson, K.; Gull, T. New forbidden and fluorescent Fe III lines identified in HST spectra of eta Carinae. *Astron. Astrophys.* **2000**, *361*, 977–981.
53. Badnell, N.R. A Breit-Pauli distorted wave implementation for AUTOSTRUCTURE. *Comput. Phys. Commun.* **2011**, *182*, 1528–1535. https://doi.org/10.1016/j.cpc.2011.03.023.
54. Parpia, F.A.; Fischer, C.F.; Grant, I.P. GRASP92: A package for large-scale relativistic atomic structure calculations. *Comput. Phys. Commun.* **1996**, *94*, 249–271. https://doi.org/10.1016/0010-4655(95)00136-0.
55. Kramida, A.; Yu. Ralchenko.; Reader, J.; NIST ASD Team. *NIST Atomic Spectra Database*, version 5.9; National Institute of Standards and Technology: Gaithersburg, MD, USA, 2021.
56. Hibbert, A.; Glass, R.; Froese Fischer, C. A general program for computing angular integrals of the Breit-Pauli Hamiltonian. *Comput. Phys. Commun.* **1991**, *64*, 455–472. https://doi.org/10.1016/0010-4655(91)90138-B.
57. Mendoza, C.; Bautista, M.A.; Deprince, J.; García, J.A.; Gatuzz, E.; Gorczyca, T.W.; Kallman, T.R.; Palmeri, P.; Quinet, P.; Witthoeft, M.C. The XSTAR Atomic Database. *Atoms* **2021**, *9*, 12. https://doi.org/10.3390/atoms9010012.
58. Storey, P.J.; Sochi, T. Electron temperatures and free-electron energy distributions of nebulae from C II dielectronic recombination lines. *Mon. Not. R. Astron. Soc.* **2013**, *430*, 599–610. https://doi.org/10.1093/mnras/sts660.
59. Sochi, T. Atomic and Molecular Aspects of Astronomical Spectra. PhD thesis, University College London, UK, 2012.
60. Peimbert, A. The Chemical Composition of the 30 Doradus Nebula Derived from Very Large Telescope Echelle Spectrophotometry. *Astrophys. J.* **2003**, *584*, 735–750. https://doi.org/10.1086/345793.
61. García-Rojas, J.; Esteban, C.; Peimbert, A.; Peimbert, M.; Rodríguez, M.; Ruiz, M.T. Deep echelle spectrophotometry of S 311, a Galactic HII region located outside the solar circle. *Mon. Not. R. Astron. Soc.* **2005**, *362*, 301–312. https://doi.org/10.1111/j.1365-2966.2005.09302.x.
62. García-Rojas, J.; Esteban, C.; Peimbert, M.; Costado, M.T.; Rodríguez, M.; Peimbert, A.; Ruiz, M.T. Faint emission lines in the Galactic H II regions M16, M20 and NGC 3603. *Mon. Not. R. Astron. Soc.* **2006**, *368*, 253–279. https://doi.org/10.1111/j.1365-2966.2006.10105.x.
63. García-Rojas, J.; Esteban, C.; Peimbert, A.; Rodríguez, M.; Peimbert, M.; Ruiz, M.T. The chemical composition of the Galactic H II regions M8 and M17. A revision based on deep VLT echelle spectrophotometry. *Rev. Mex. Astron. Astrofis.* **2007**, *43*, 3–31.
64. López-Sánchez, Á.R.; Esteban, C.; García-Rojas, J.; Peimbert, M.; Rodríguez, M. The Localized Chemical Pollution in NGC 5253 Revisited: Results from Deep Echelle Spectrophotometry. *Astrophys. J.* **2007**, *656*, 168–185. https://doi.org/10.1086/510112.

65. Esteban, C.; Bresolin, F.; Peimbert, M.; García-Rojas, J.; Peimbert, A.; Mesa-Delgado, A. Keck HIRES Spectroscopy of Extragalactic H II Regions: C and O Abundances from Recombination Lines. *Astrophys. J.* **2009**, *700*, 654–678. https://doi.org/10.1088/0004-637X/700/1/654.
66. Esteban, C.; García-Rojas, J.; Carigi, L.; Peimbert, M.; Bresolin, F.; López-Sánchez, A.R.; Mesa-Delgado, A. Carbon and oxygen abundances from recombination lines in low-metallicity star-forming galaxies. Implications for chemical evolution. *Mon. Not. R. Astron. Soc.* **2014**, *443*, 624–647. https://doi.org/10.1093/mnras/stu1177.
67. Esteban, C.; Fang, X.; García-Rojas, J.; Toribio San Cipriano, L. The radial abundance gradient of oxygen towards the Galactic anti-centre. *Mon. Not. R. Astron. Soc.* **2017**, *471*, 987–1004. https://doi.org/10.1093/mnras/stx1624.
68. Esteban, C.; Bresolin, F.; García-Rojas, J.; Toribio San Cipriano, L. Carbon, nitrogen, and oxygen abundance gradients in M101 and M31. *Mon. Not. R. Astron. Soc.* **2020**, *491*, 2137–2155. https://doi.org/10.1093/mnras/stz3134.
69. Esteban, C.; García-Rojas, J. Revisiting the radial abundance gradients of nitrogen and oxygen of the Milky Way. *Mon. Not. R. Astron. Soc.* **2018**, *478*, 2315–2336. https://doi.org/10.1093/mnras/sty1168.
70. Domínguez-Guzmán, G.; Rodríguez, M.; García-Rojas, J.; Esteban, C.; Toribio San Cipriano, L. The homogeneity of chemical abundances in H II regions of the Magellanic Clouds. *Mon. Not. R. Astron. Soc.* **2022**, *517*, 4497–4514. https://doi.org/10.1093/mnras/stac2974.
71. Verner, E.M.; Verner, D.A.; Korista, K.T.; Ferguson, J.W.; Hamann, F.; Ferland, G.J. Numerical Simulations of Fe II Emission Spectra. *Astrophys. J. Suppl. Ser.* **1999**, *120*, 101–112. https://doi.org/10.1086/313171.
72. Rodríguez, M. Fluorescence of [Fe II] in H II regions. *Astron. Astrophys.* **1999**, *348*, 222–226.
73. Verner, E.M.; Verner, D.A.; Baldwin, J.A.; Ferland, G.J.; Martin, P.G. Continuum Pumping of [Fe II] in the Orion Nebula. *Astrophys. J.* **2000**, *543*, 831–839. https://doi.org/10.1086/317159.
74. Hartman, H. Fluorescence in Astrophysical Plasmas. In *New Trends in Atomic and Molecular Physics*; Springer: Berlin/Heidelberg, Germany, 2013; p. 189. https://doi.org/10.1007/978-3-642-38167-6_11.
75. Sarkar, A.; Ferland, G.J.; Chatzikos, M.; Guzmán, F.; van Hoof, P.A.M.; Smyth, R.T.; Ramsbottom, C.A.; Keenan, F.P.; Ballance, C.P. Improved Fe II Emission-line Models for AGNs Using New Atomic Data Sets. *Astrophys. J.* **2021**, *907*, 12. https://doi.org/10.3847/1538-4357/abcaa6.